



Simon Prato

Numerical Investigation of TEM Cells and Antenna Coupling

Master Thesis

Studies: Electrical Engineering

submitted to

Technical University of Graz

Supervisor

Dr. Thomas Bauernfeind



Graz, August 2024

Abstract

Contents

1	Introduction	1
2	Dipole Theory	1
2.1	Electric Dipoles	1
2.1.1	Infinitesimal Electric Dipoles	1
2.1.2	Small Electric Dipoles	3
2.2	Magnetic Dipoles	6
2.2.1	Crossed Dipoles	7
2.3	Antennas to Investigate	7
2.3.1	IFA	7
2.3.2	Center fed monopole antenna	7
2.4	Crossed dipole antenna	7
2.5	Radiated Field	8
2.6	Antenna Terminology	8
2.7	Field regions	8
2.8	Radiated Power	10
3	Guided Waves	10
3.1	Lorentz Reciprocity Theorem	10
3.2	Green's Function	11
3.2.1	Scalar Green's Function	11
3.2.2	Dyadic Green's Function	12
3.3	Modes in TEM Cells	13
3.3.1	Power transfer of modes	13
3.3.2	Modes in rectangular waveguides	14
3.3.3	TEM Mode in TEM Cells	15
3.3.4	Higher order modes in TEM cells	18
3.4	Electrically Small Radiating Sources in TEM Cells	20
3.5	Shielding	24
3.5.1	ASTM ES7-83 Method	26
3.5.2	Dual TEM cell	27
4	Numerical Investigations	28
4.1	Finite Element Method	28
4.1.1	General Idea	28
4.1.2	Dividing a computational domain into finite elements	29
4.1.3	Solving the differential equation	31
4.1.4	Adaptive solution process	32
4.2	Antennas	32
4.2.1	Inverted F-antenna	33
4.2.2	Center Fed Monopole Antenna	40
4.2.3	Monopole Antenna	41
4.2.4	Loop antenna	43
4.2.5	Serial Loop Antenna	50

4.2.6	Offset of source antennas and eddy currents	51
4.3	Dipole Moments	52
4.3.1	Orientation and position in TEM Cell	52
4.3.2	Combining dipole moments with antennas	54
4.3.3	Application of dipole moments	54
4.4	Investigation of field regions	54
4.5	Shielding Simulations	56
4.5.1	Shielding effectiveness of graphite	56
4.5.2	Shield effectiveness of FR4	57
4.5.3	Dual TEM Cell	57

List of Figures

2.1	Geometrical arrangement of an infinitesimal electric dipole. It contains a capacitor-plate at each end of the wire to provide a constant current $\mathbf{I}(z)$.	2
2.2	Geometrical arrangement of a linear, center-fed wire antenna with a feed-point indicated in the center. The feedpoint consists of a small gap providing current I_0 to the antenna.	4
2.3	Current distribution across linear wire antenna. It has a maximum at the feedpoint, and drops to zero at points $d/2$ and $-d/2$.	5
2.4	Geometrical arrangement of a current loop fed by a current I_0 , producing a magnetic dipole moment. Alternatively, a magnetic current I_m flows perpendicular to the loop's area along the distance L , which produces an equivalent magnetic dipole moment.	7
2.5	Field regions of an antenna [2]	9
2.6	Magnitude of the terms $1/(kr)$ and $1/(kr)^2$ depending on distance r [2]	10
3.1	TEM cell with vertical antenna inserted	16
3.2	Cross section of the TEM cell	18
3.3	Propagation of TEM, TE ₀₁ and TE ₁₀ modes in TEM cell	19
3.4	Transversal electric fields in cross section of TEM cell	20
3.5	Normalized e-field distribution along z-axis at center of septum for visualization, where the y-axis is the magnitude and the x-axis is the point in the height position in the TEM cell.	23
3.6	TODO: This is how the dimensions in these formulas are defined in [30]	23
3.7	Output power and norm. E-field over offset	24
3.8	Output power and norm. E-field over height	24
3.9	Incident, reflected and transmitted electric fields due to interaction with shielding material	24
3.11	Dual TEM cell with aperture	28
4.1	Tetrahedron with points on the edge and vertices.	29
4.2	Face of the finite element with unknowns	30
4.3	Adaptive solution process	32
4.4	Inverted F-antenna used in the simulation	33
4.5	S-parameter describing coupling of antenna to waveport 1	33
4.6	Phase of S-parameters from antenna to waveport 1 and 2	35
4.7	Dipole moments and measurement point of $e_{0,z}$ in TEM cell	36
4.8	Dipole moments over frequency	37
4.9	Output power and electric field over frequency	38
4.10	Phase of S-parameters from rotated antenna to waveport 1 and 2	38
4.11	Dipole moments of rotated antenna	39
4.12	Center fed monopole antenna used in simulation	40
4.13	S-parameter describing coupling of antenna to waveport 1	40
4.14	Phase shift	41
4.15	Dipole moments	41
4.16	Dipole moments	41
4.17	Phase shift	41
4.18	Current surface density at 550 MHz	42

4.19	Current surface density at 550 MHz with offset	42
4.20	Chu equivalent circuit of short dipole	43
4.21	Current distribution	43
4.22	Feed current	43
4.23	Dipole moments of loop antenna	44
4.24	Surface current density at 550 MHz	45
4.25	Surface current density at 550 MHz with offset	45
4.26	Surface current density at 550 MHz with rotated antenna	46
4.27	Surface current density at 550 MHz with offset and rotated antenna	46
4.28	Charge density distribution in current loop antenna	46
4.29	Current density distribution in current loop antenna	46
4.30	Electric near field in current loop antenna	47
4.31	Magnetic near field in current loop antenna	47
4.32	Voltage drop at feed point of current loop antenna	47
4.33	Current consumption at feed point of current loop antenna	47
4.34	Wave impedance in the center of the loop	48
4.35	Power consumption of the current loop antenna	48
4.36	Total power distribution in the system	49
4.37	Wave impedance in near field of loop antenna over frequency	50
4.38	Serial loop antenna	50
4.39	Dipole moments	51
4.40	CFM S11 sweep with rotation angle stepping	52
4.41	Center fed monopole antenna coupling dependence on offset (Delete after) .	52
4.42	Comparison of normalized output power of electric dipole moments	53
4.43	TEM cell containing dipole moments	54
4.44	Moments in small TEM cell	55
4.45	Moments in normal TEM cell	55
4.46	$k \cdot r$ in small TEM cell	55
4.47	$k \cdot r$ for other TEM cells	55
4.48	Output powers	56
4.49	Phase shifts	56
4.50	Shielding effectiveness of graphite	56

List of Tables

1	Cut-off frequencies of higher order modes depending on TEM cell dimensions	20
2	Forward transmission coefficients	57

1 Introduction

2 Dipole Theory

Magnetic and electric dipoles are an effective approach for modeling the radiation of electrically small antennas. They are defined as antennas with dimensions much less than one-tenth of the wavelength ($l \ll \lambda$)[2, p. 151]. By calculating the respective dipole moments, the coupling between antennas and TEM cells can be numerically estimated. This section provides a brief introduction to the underlying theory of this concept.

Explanation
Dipole
Moments
modeling,
antennas
and fields

2.1 Electric Dipoles

2.1.1 Infinitesimal Electric Dipoles

An electric dipole can be modeled as two tiny charged metal spheres or two capacitor-plates connected by a linear wire of length d and diameter a [8, p. 467], [2, p. 151]. The charges accelerate along the wire and radiate. In case of an ideal, infinitesimal dipole, the wire is very thin ($a \ll \lambda$) and very small ($d \ll \lambda$) compared to the wavelength λ [2, p. 151], [8, p. 468]. For an antenna to be accurately modeled as an infinitesimal electric dipole, its length usually must be smaller than a fiftieth of the wavelength ($d < \lambda/50$) [2, p. 156]. They are not very practical, but serve as a basic building block for more complex geometries or as a useful excitation method in numerical investigations.

An electric dipole is shown in Figure 2.1 and will now be analyzed. The dipole is aligned with the z-axis, which simplifies the mathematical calculations. Time variation according to $e^{-j\omega t}$ is assumed and therefore omitted. A current flows in the wire, which is spatially uniform throughout the wire. This is expressed as [2, p. 151]

$$\mathbf{I}(z) = \hat{\mathbf{a}}_z I_0. \quad (1)$$

The capacitances modeled at the end of the wire enable the constant current flow, which would otherwise be physically impossible. Next, the vector potential \mathbf{A} is determined through the general expression

$$\mathbf{A}(\mathbf{x}) = \frac{\mu}{4\pi} \frac{e^{-jkr}}{r} \iiint_V \mathbf{J}(\mathbf{x}') d\mathbf{x}'. \quad (2)$$

The vector $\mathbf{x} = \hat{\mathbf{a}}_x x + \hat{\mathbf{a}}_y y + \hat{\mathbf{a}}_z z$ represents the observation point coordinates, while $\mathbf{x}' = \hat{\mathbf{a}}_x x' + \hat{\mathbf{a}}_y y' + \hat{\mathbf{a}}_z z'$ represents the source point coordinates. The vectors $\hat{\mathbf{a}}_x$, $\hat{\mathbf{a}}_y$, and $\hat{\mathbf{a}}_z$ are unit vectors along the x-, y-, and z-directions, respectively. \mathbf{J} is the current density in the source region. The variable r is the distance from any source point to the observation point $|\mathbf{x} - \mathbf{x}'|$. In this case, the source point $\mathbf{x}' = \mathbf{0}$, due to the infinitesimal dipole [2, p. 152]. The permeability is described by μ and the propagation of the wave by e^{jkr} , where $k = 2\pi/\lambda$ is the propagation factor, or often called wavenumber.

The integration is performed over the volume V of the antenna. This leads to [2, p. 153]

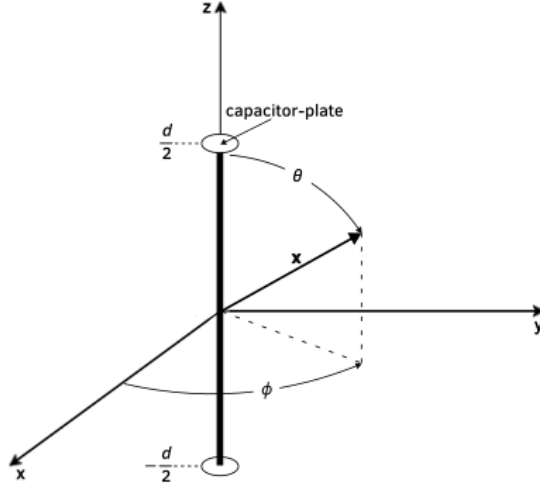


Figure 2.1 Geometrical arrangement of an infinitesimal electric dipole. It contains a capacitor-plate at each end of the wire to provide a constant current $\mathbf{I}(z)$.

$$\mathbf{A}(\mathbf{x}) = \hat{\mathbf{a}}_z \frac{\mu I_0}{4\pi r} e^{-jkr} \int_{-d/2}^{+d/2} dz' = \hat{\mathbf{a}}_z \frac{\mu I_0 d}{4\pi r} e^{-jkr}. \quad (3)$$

Any other field quantities can be derived out of the vector potential \mathbf{A} , such as the electric field intensity \mathbf{E} and magnetic field intensity \mathbf{H} . To simplify this process, the Cartesian components of \mathbf{A} are first transformed into spherical ones. This transform is given in matrix form as [2, p. 153]

$$\begin{bmatrix} A_r \\ A_\theta \\ A_\phi \end{bmatrix} = \begin{bmatrix} \sin \theta \cos \phi & \sin \theta \sin \phi & \cos \theta \\ \cos \theta \cos \phi & \cos \theta \sin \phi & -\sin \theta \\ -\sin \phi & \cos \phi & 0 \end{bmatrix} \begin{bmatrix} A_x \\ A_y \\ A_z \end{bmatrix}, \quad (4)$$

where θ is the polar angle and ϕ is the azimuthal angle of the observation point \mathbf{x} . \mathbf{E} and \mathbf{H} are then expressed by [2, p. 153],

$$\mathbf{H} = \frac{1}{\mu r} \left[\frac{\partial}{\partial r} (r A_\theta) - \frac{\partial A_r}{\partial \theta} \right] \hat{\mathbf{a}}_\phi, \quad (5a)$$

$$\mathbf{E} = -j\omega \mathbf{A} - j \frac{1}{\omega \mu \epsilon} \nabla (\nabla \cdot \mathbf{A}). \quad (5b)$$

Substituting \mathbf{A} into Equations (5a) and (5b) reduces them to

$$E_r = \eta \frac{I_0 d \cos \theta}{2\pi r^2} \left[1 + \frac{1}{jkr} \right] e^{-jkr}, \quad (6a)$$

$$E_\theta = j\eta \frac{kI_0 d \sin \theta}{4\pi r} \left[1 + \frac{1}{jkr} - \frac{1}{(kr)^2} \right] e^{-jkr}, \quad (6b)$$

$$E_\phi = 0. \quad (6c)$$

and,

$$H_r = H_\theta = 0, \quad (7a)$$

$$H_\phi = j \frac{kI_0 d \sin \theta}{4\pi r} \left[1 + \frac{1}{jkr} \right] e^{-jkr}, \quad (7b)$$

$\eta = \sqrt{\frac{\mu}{\epsilon}}$ is the wave impedance of the medium in which the waves travel.

The total radiated power of the dipole is obtained by integrating the complex Poynting vector \mathbf{W} over a closed surface surrounding the dipole [2, p. 154]. The real part of the total radiated power provides information about energy transferred by radiation, while the imaginary part about the antenna's reactive behavior. \mathbf{W} is defined by

$$\mathbf{W} = \frac{1}{2} (\mathbf{E} \times \mathbf{H}^*). \quad (8)$$

The real power transfer is derived through the time-averaged Poynting vector \mathbf{W}_{av} [2, p. 160], which is calculated by

$$\mathbf{W}_{av} = \frac{1}{2} \Re\{\mathbf{E} \times \mathbf{H}^*\}. \quad (9)$$

By integrating the time-averaged real Poynting vector \mathbf{W}_{av} over a closed surface, the radiated power P_{rad} is determined. The real part of the power is independent of the integrated surface, opposed to the imaginary part. P_{rad} is expressed as [2, p. 155]

$$P_{rad} = \eta \left(\frac{\pi}{3} \right) \left| \frac{I_0 l}{\lambda} \right|^2 \quad (10)$$

The radiated power increases, at least in the near-field region, with the frequency squared [12, p. 412]. This relation holds until the frequency is too large to consider the antenna as electrically small.

2.1.2 Small Electric Dipoles

Wires that are too long to be modeled as an infinitesimal dipole, but short enough to be considered electrically small ($\lambda/50 < l \leq \lambda/10$), are classified as small physical dipoles [2, pp. 162-163]. They are a more accurate and useful representation of a linear wire antenna, and now investigated further.

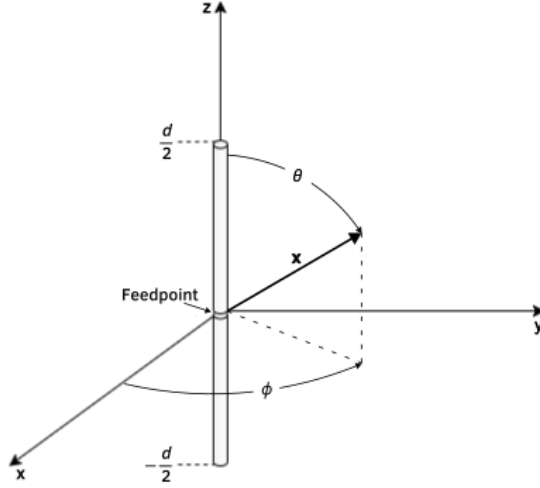


Figure 2.2 Geometrical arrangement of a linear, center-fed wire antenna with a feed-point indicated in the center. The feedpoint consists of a small gap providing current I_0 to the antenna.

A current I_0 is fed into the short, center-fed, linear antenna shown in Figure 2.1. The current along the antenna arms $I(z)$ linearly drops to zero [12, p. 412], as visualized in Figure 2.3. Mathematically, it is described by,

$$\mathbf{I}(z) = \hat{\mathbf{a}}_z I_0 \left(1 - \frac{2|z|}{d} \right). \quad (11)$$

This is different to the current distribution of the infinitesimal dipole. The capacitor-plates are therefore not needed in this model. Furthermore, charge accumulates along the antenna due to the linear drop of current \mathbf{I} . It is expressed as a charge per unit length ρ' , which is appropriate due to the thin wire. It is derived by the continuity equation $j\omega\rho = \nabla \cdot \mathbf{J}$, which leads to [12, pp. 410-412]

$$\rho' = \pm \frac{d}{dz} j \frac{I(z)}{\omega} = \pm j \frac{2I_0}{\omega d}. \quad (12)$$

ρ' is uniformly distributed along each antenna arm.

An important metric is the electric dipole moment \mathbf{p} . It is defined as the product of charge density ρ along the antenna and their source point \mathbf{x}' [12, p.410], and generally expressed as

$$\mathbf{p} = \iiint_V \mathbf{x}' \rho(\mathbf{x}') d\mathbf{x}'. \quad (13)$$

The charge distribution ρ' enables the calculation of the electric dipole moment \mathbf{p} , which results in

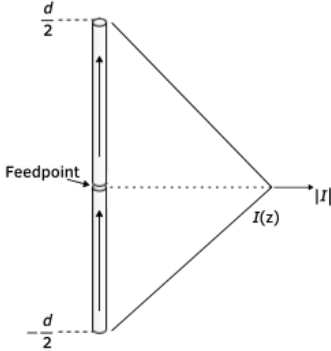


Figure 2.3 Current distribution across linear wire antenna. It has a maximum at the feedpoint, and drops to zero at points $d/2$ and $-d/2$.

$$\mathbf{p} = \int_{-\frac{d}{2}}^{\frac{d}{2}} z\rho'(z) dz \cdot \hat{\mathbf{a}}_z = j \frac{I_0 d}{2\omega} \cdot \hat{\mathbf{a}}_z. \quad (14)$$

The electric dipole moment \mathbf{p} is parallel to the antenna's arms and points in the z -direction [12, p. 412], [8, p. 155]. Next, the vector potential \mathbf{A} is determined using Equation 2. The calculations of \mathbf{A} simplify to [12, p. 410],

$$\mathbf{A}(\mathbf{x}) = -j \frac{\mu\omega}{4\pi} \mathbf{p} \frac{e^{-jkr}}{r} \quad (15)$$

The formulation of \mathbf{A} now contains an additional factor of $1/2$, compared to the previously derived \mathbf{A} of the infinitesimal dipoles in Equation 3. This is due to the integration process of \mathbf{I} . When integrated over the same interval $[-d/2, d/2]$, the linearly dropping \mathbf{I} yields half the value of a constant \mathbf{I} . Furthermore, it makes sense to keep $\mathbf{x}' = \mathbf{0}$ for simplicity reasons. It has been shown, that this approximation is sufficient for large r , and the amplitude error remains negligible for small r [12, p. 409], [2, pp. 164-168].

The electric field intensity \mathbf{E} , the magnetic field intensity \mathbf{H} and the radiated power P_{rad} can be derived analogous to the infinitesimal dipole. P_{rad} is expressed as [2, p. 165]

$$P_{\text{rad}} = \eta \left(\frac{\pi}{12} \right) \left| \frac{I_0 l}{\lambda} \right|^2 \quad (16)$$

and is also smaller by a factor of $1/4$ compared to P_{rad} of the infinitesimal dipole in Equation 10.

The short physical electric dipole described in this section approximate the behavior of electrically short antennas. Special care must be taken of the excitation method and shape, as it influences the behavior [12, p. 413]. Additionally, any antenna investigated through this method must remain as small as possible compared to the wavelength λ , to reduce any analytical approximation errors.

This makes it reasonable to model electrically small antennas with infinitesimal dipoles

Image theory may be added for TEM cell explanations [Balanis]

2.2 Magnetic Dipoles

The magnetic dipole moment characterizes the strength of a magnetic source. A small current loop fed with a current I_0 can be used to model the magnetic dipole, as demonstrated in Figure 2.4. This relation holds as long as its overall length is smaller than a tenth of the wavelength ($2b\pi < \lambda/10$) and as long as the wire is very thin [2, p. 231]. Furthermore, the radiation pattern of the magnetic dipole is equal to that of the electric dipole, with the role of the electric and magnetic fields interchanged [8, p. 254].

The magnetic dipole moment \mathbf{m} is given by [12, p. 413]

$$\mathbf{m} = \frac{1}{2} \iiint_V (\mathbf{x}' \times \mathbf{J}) d\mathbf{x}'. \quad (17)$$

Furthermore, the magnetic current I_m and the electric current I_0 in the loop are related with [2, p. 237]

$$I_m L = jA\omega\mu_0 I_0 \quad (18)$$

with $A = b^2\pi$ being the area of the current loop. Analogous to the separation distance d in the electric dipole, L is the length of the magnetic dipole. I_m and L may be used to model the magnetic dipole moment instead of the current loop. The fields \mathbf{E} and \mathbf{H} generated are the same in both cases. This means, that the infinitesimal magnetic dipole can be replaced with an electrically small loop [2, p. 237]. This was not the case for the infinitesimal and electrically small electric dipoles. \mathbf{E} and \mathbf{H} of the magnetic dipole moment or electrically small current loop are then determined with [2, p. 237]

$$E_r = E_\theta = 0, \quad (19a)$$

$$E_\phi = -j \frac{kI_m d \sin \theta}{4\pi r} \left[1 + \frac{1}{jkr} \right] e^{-jkr}, \quad (19b)$$

and,

$$H_r = \frac{I_m d \cos \theta}{2\pi r^2 \eta} \left[1 + \frac{1}{jkr} \right] e^{-jkr}, \quad (20a)$$

$$H_\theta = j \frac{kI_m d \sin \theta}{4\pi r \eta} \left[1 + \frac{1}{jkr} - \frac{1}{(kr)^2} \right] e^{-jkr}, \quad (20b)$$

$$H_\phi = 0. \quad (20c)$$

The complex power density \mathbf{W} can be derived analogous to the the electric dipole case in Equation 8. For the magnetic dipole, the imaginary part of \mathbf{W} has the opposite sign

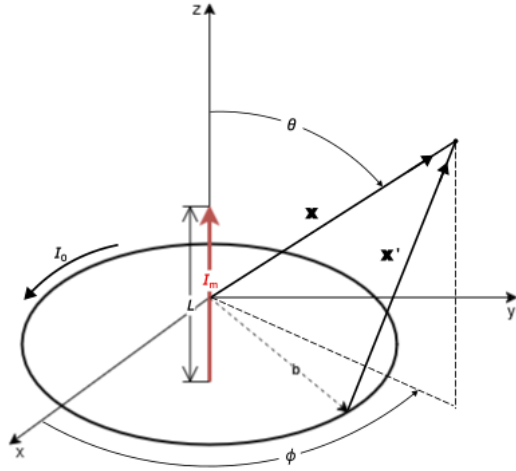


Figure 2.4 Geometrical arrangement of a current loop fed by a current I_0 , producing a magnetic dipole moment. Alternatively, a magnetic current I_m flows perpendicular to the loop's area along the distance L , which produces an equivalent magnetic dipole moment.

compared to the electric dipole. This is the result of the near-field power being inductive in case of the magnetic dipole, while it is capacitive for the electric dipole [2, p. 238].

The radiated power P_{rad} of the small current loop is given by [2, p. 238]

$$P_{\text{rad}} = \eta \left(\frac{\pi}{12} \right) (kb)^4 |I_0|. \quad (21)$$

2.2.1 Crossed Dipoles

Crossed dipoles can generate a wide variety of radiation patterns. Supposed two dipoles are placed perpendicular to each other and fed 90° out of phase, an omnidirectional radiation pattern is created [27]. If the equivalent dipoles of an EUT represents such two dipoles, any mode which can propagate in the TEM cell will do so, and therefore influence the measurement result. It is therefore not only important to know which dipoles there are representing the EUT, but also what phase and magnitude they have. Meaning that not only the dipoles aligned with the TEM mode alone influence the result.

Write

Dipoles next to conducting planes (balanis, collin)

2.3 Antennas to Investigate

2.3.1 IFA

2.3.2 Center fed monopole antenna

2.4 Crossed dipole antenna

A crossed dipole antenna radiates very evenly into every direction. This could be interesting to use, in order to excite several modes, especially in the presence of shielding materials.

When this antenna is near a perfect electric conductor (PEC), the gain becomes dependent on the distance to it. At a distance of $H = 0.25\lambda$, the gain reaches a maximum due to constructive interference in normal direction to the PEC surface. When the distance is small, the image currents may cancel and the gain decreases. Therefore, the output power on the TEM cells depends on the distance, and implicitly on the frequency. This means that the frequency behavior of the representing dipoles may vary from a standard dipole.

Additionally, when a shielding material is present, different modes may be excited, which also influence the behavior. Those different modes depend on all 6 dipole moments, with which the antenna shall be modeled.

2.5 Radiated Field

2.6 Antenna Terminology

Is this chapter necessary?

2.7 Field regions

The field quantities \mathbf{E} and \mathbf{H} have been derived for an infinitesimal electric dipole in Equations (6a) to (6c) and Equations (7a) and (7b). They are valid everywhere except for the source region [2, p. 156]. Depending on the distance r to the dipole, the behavior of the fields changes. This becomes apparent when investigating E_θ in Equation 6b, specifically expressions 1 and 2 in

$$E_\theta = j\eta \frac{kI_0d \sin \theta}{4\pi r} \left[1 + \underbrace{\frac{1}{jkr}}_{\text{expression 1}} - \underbrace{\frac{1}{(kr)^2}}_{\text{expression 2}} \right] e^{-jkr}. \quad (22)$$

If the distance $r < \lambda/2\pi$ ($kr < 1$), then expression 2 dominates the value in the brackets. Consequently, the energy stored in this region is mostly imaginary. It is referred to as the near-field region.

At $r = \lambda/2\pi$ ($kr = 1$), expression 1 and 2 are of equal magnitude. This leads to the energy stored

Continue

The region around an antenna may be divided into three sub-regions:

- Reactive near-field region
- Radiating near-field or Fresnel region
- Far-field or Fraunhofer region

They are shown in Figure 2.5. These regions are distinguished for most antennas using the wavelength λ and the largest dimension of the antenna D . The nearest region to the antenna, the reactive near-field region, is a sphere with radius R_1 , which is calculated with Equation 23a. It is characterized by the predominantly reactive fields in it. The next region, the radiating near-field region, is located around the first, within a sphere of radius

R_2 calculated in Equation 23b. In there, the radiating fields dominate and the angular field distribution is dependent on the distance to the antenna. In the largest and last region, the far-field region, the angular field distribution is independent of the distance to the antenna [2].

$$R_1 = 0.62\sqrt{D^3/\lambda} \quad (23a)$$

$$R_2 = 2D^2/\lambda \quad (23b)$$

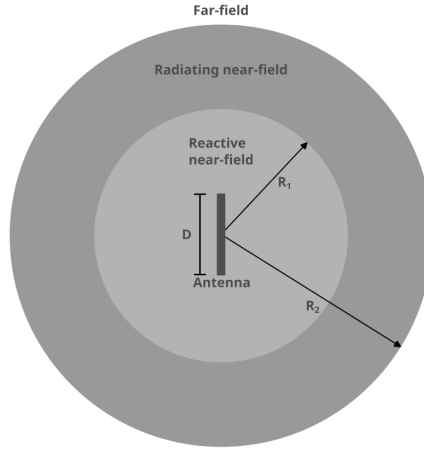


Figure 2.5 Field regions of an antenna [2]

The electrically short antennas located in the TEM cell interact with it mostly through the reactive near-field region. However, if the TEM cell is large and frequencies are high, the coupling occurs over the radiating near-field. There, the field distributions are different, hence the dipole moments couple differently over frequency to the cell.

Is this even possible without reaching other modes behavior? And demonstrate the fields over frequency and distance, which changes differently in different regions

An infinitesimal dipole is taken as an antenna. The fields are calculated through the auxiliary fields, as described earlier by Equation 5, which leads to Equation 24 for the magnetic field strength and Equation 25 for the electric field strength. Those equations are valid everywhere, except for the source point [2].

$$H_r = H_\theta = 0 \quad (24a)$$

$$H_\phi = j \frac{kI_0l \sin \theta}{4\pi r} \left[1 + \frac{1}{jkr} \right] e^{-jkr} \quad (24b)$$

$$E_r = n \frac{I_0l \cos \theta}{2\pi r^2} \left[1 + \frac{1}{jkr} \right] e^{-jkr} \quad (25a)$$

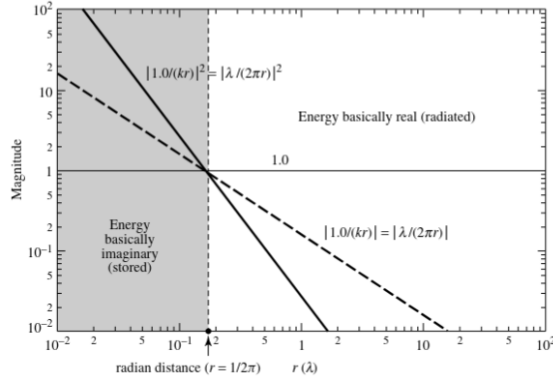


Figure 2.6 Magnitude of the terms $1/(kr)$ and $1/(kr)^2$ depending on distance r [2]

$$E_\theta = j\eta \frac{kI_0 l \sin \theta}{4\pi r} \left[1 + \frac{1}{jkr} - \frac{1}{(kr)^2} \right] e^{-jkr} \quad (25b)$$

$$E_\phi = 0 \quad (25c)$$

The distance of $\lambda/2\pi$, leading to $kr = 1$, is called radian distance, where r is the distance to the antenna and k is the free-space wave number. There, the real and imaginary part for both H_ϕ and E_r is equal. Furthermore in E_θ , only the $1/(jkr)$ term contributes to the field, because the other terms cancel each other out. The radian distance essentially marks a point of equal imaginary and stored power [2].

In distances smaller than the radian distance $kr < 1$, the fields are largely reactive and located in a reactive near-field region. There, the field strength decreases with the cube of the distance ($\propto 1/r^3$). At distances beyond the radian distance ($kr \geq 1$), in the intermediate-field region, the field strength decreases with the square of the distance ($\propto 1/r^2$) [2]. This behavior is visualized in Figure 2.6.

The wave-number k is dependent on the frequency. Therefore, when placing an infinitesimal dipole into a TEM cell, its coupling behavior depends on the distance and the field regions, that couple. For that reason, the kr number shall be investigated over the whole frequency range for different distances.

2.8 Radiated Power

Important for the Lorentz Reciprocity Part.

3 Guided Waves

3.1 Lorentz Reciprocity Theorem

The Lorentz reciprocity theorem proves to be very useful, hence it is summarized here. It states that any two fields $\mathbf{E}_1, \mathbf{H}_1$ and $\mathbf{E}_2, \mathbf{H}_2$, which are of the same frequency and

in linear and isotropic media, can be expressed by its differential form in Equation 26 [2, 6]. Here, \mathbf{J} describes the electric current density with the unit $\frac{\text{A}}{\text{m}^2}$ and \mathbf{M} the magnetic current density with the unit $\frac{\text{V}}{\text{m}^2}$. They act as sources, exciting the electric and magnetic fields \mathbf{E} and \mathbf{H} . The theorem says, that under the previously described conditions, any source and response can be locally interchanged, and the results would remain the same.

$$-\nabla \cdot (\mathbf{E}_1 \times \mathbf{H}_2 - \mathbf{E}_2 \times \mathbf{H}_1) = \mathbf{E}_1 \cdot \mathbf{J}_2 + \mathbf{H}_2 \cdot \mathbf{M}_1 - \mathbf{E}_2 \cdot \mathbf{J}_1 - \mathbf{H}_1 \cdot \mathbf{M}_2 \quad (26)$$

By taking a volume integral of both sides of Equation 26 and using the divergence theorem, Equation 27 emerges [2, 6].

$$\oint\oint(\mathbf{E}_1 \times \mathbf{H}_2 - \mathbf{E}_2 \times \mathbf{H}_1) \cdot dS \mathbf{n} = \iiint \mathbf{E}_1 \cdot \mathbf{J}_2 + \mathbf{H}_2 \cdot \mathbf{M}_1 - \mathbf{E}_2 \cdot \mathbf{J}_1 - \mathbf{H}_1 \cdot \mathbf{M}_2 \cdot dV \quad (27)$$

If there aren't any sources present, meaning that $\mathbf{J}_1 = \mathbf{J}_2 = \mathbf{M}_1 = \mathbf{M}_2 = 0$, the Lorentz reciprocity theorem simplifies to Equation 28 [2, 21]. This is especially useful for free wave propagation of antennas.

$$-\nabla \cdot (\mathbf{E}_1 \times \mathbf{H}_2 - \mathbf{E}_2 \times \mathbf{H}_1) = 0 \quad (28)$$

Another application arises when investigating a volume V confined by a perfectly conducting surface S , through which two linear current densities \mathbf{J}_1 and \mathbf{J}_2 flow. Because $\mathbf{n} \times \mathbf{E}_1 = \mathbf{n} \times \mathbf{E}_2 = 0$ along the surface S , the surface integral in Equation 27 equals zero, and Equation 29 arises. This is the Rayleigh-Carson form of the Lorentz reciprocity theorem and is particularly useful for deriving waveguide modes and constructing the respective fields [6].

$$\mathbf{E}_1 \cdot \mathbf{J}_2 = \mathbf{E}_2 \cdot \mathbf{J}_1 \quad (29)$$

3.2 Green's Function

3.2.1 Scalar Green's Function

Green's function describes the response of a linear differential operator L to a point source as an input, which is modeled by delta-function δ . Its general form is shown in Equation 30.

$$LG(\mathbf{x}, \mathbf{x}') = \delta(\mathbf{x} - \mathbf{x}') \quad (30)$$

Once Equation 30 is solved and the Green's function G of this specific operator is known, it can be used to solve any input function, such as $u(\mathbf{x})$ in Equation 31a. This is done by a convolution integral, shown in Equation 31b.

$$Lu(\mathbf{x}) = f(\mathbf{x}) \quad (31a)$$

$$u(\mathbf{x}) = \int G(\mathbf{x}, \mathbf{x}') f(\mathbf{x}') d\mathbf{x}' \quad (31b)$$

The Green's function can be used to solve equations involving the Nabla operator ∇ in electrostatics. Equation 32a and Equation 32b demonstrate how the scalar potential ϕ can be calculated from point charge distributions in space ρ by using the Green's function of the Nabla operator. There, the Green's function $G(\mathbf{x}, \mathbf{x}') = \frac{1}{4\pi|\mathbf{x}-\mathbf{x}'|}$ represents the potential at position \mathbf{x} created by an unit point charge at point \mathbf{x}' .

$$\nabla \phi = -\frac{\rho}{\epsilon_0} \quad (32a)$$

$$\phi(\mathbf{x}) = \frac{1}{4\pi\epsilon_0} \iiint_V \frac{\rho(\mathbf{x}')}{|\mathbf{x} - \mathbf{x}'|} dV' \quad (32b)$$

When boundary conditions are present, the Green's Function may be modified to make the boundary condition vanish. The resulting function is called tailored Green's Function. This proves especially useful in the analysis of guided waves. Another possibility is to construct the Green's Function by a series of reflections on boundaries, applying image theory on perfectly conducting surfaces [6].

3.2.2 Dyadic Green's Function

The scalar Green's Function demonstrated in subsubsection 3.2.1 is useful to solve for one-dimensional functions. However, for the analysis of waveguides, the calculation of the three-dimensional vector potential \mathbf{A} as in Equation 33 is necessary.

$$\nabla^2 \mathbf{A} + k^2 \mathbf{A} = -\mu \mathbf{J} \quad (33)$$

When replacing $\mu \mathbf{J}$ by an unit vector source, the solution of the differential equation is shown in Equation 34. This is a vector Green's Function by definition.

$$(\mathbf{a}_x + \mathbf{a}_y + \mathbf{a}_z) \frac{e^{-jk|\mathbf{r}-\mathbf{r}_0|}}{4\pi|\mathbf{r}-\mathbf{r}_0|} \quad (34)$$

The solution of any current distribution \mathbf{J} can be obtained by superposition, analogous to the scalar Green's Function. A prerequisite is that each component of the current vector \mathbf{J} is each associated with one unit vector of the Green's function, i.e. J_x with \mathbf{a}_x , J_y with \mathbf{a}_y and J_z with \mathbf{a}_z . This is implemented by using a dyadic Green's Function $\hat{\mathbf{G}}$. The dyadic has a mapping function, rather than an operational one. The dyadic Green's Function is defined as the solution of Equation 35.

$$\nabla^2 \hat{\mathbf{G}}(\mathbf{r}, \mathbf{r}_0) + k^2 \hat{\mathbf{G}} = -\hat{\mathbf{I}} \delta(\mathbf{r} - \mathbf{r}_0) \quad (35)$$

Analogous to the scalar Green's Function, multiplying the unit input function by $\hat{\mathbf{I}}$ leads to the same multiplication of the Green's function, as shown in Equation 36.

$$\hat{\mathbf{G}}(\mathbf{r}, \mathbf{r}_0) = \hat{\mathbf{I}} \frac{e^{-jk|\mathbf{r}-\mathbf{r}_0|}}{4\pi|\mathbf{r}-\mathbf{r}_0|} \quad (36)$$

The dyadic Green's Function is commonly applied to calculate field distributions in waveguides. In [30] it is used to derive the fields in a TEM cell caused by a vertical current conducting wire with help of the small-gap approximation.

3.3 Modes in TEM Cells

3.3.1 Power transfer of modes

Any electromagnetic field distribution in a waveguide can be represented by an infinite series of normal modes. Equation 37 shows that each mode is orthogonal to each other, with \mathbf{e}_n^\pm and \mathbf{h}_m^\pm being the function vectors of the electric and magnetic field in transverse direction [6]. A coupling between the modes only occurs due to geometric changes of the waveguide. Additionally, each mode is normalized to \sqrt{W} , shown by Equation 38. Only the transverse fields are investigated in these Equations, because they carry power along the waveguide, opposed to the fields in the propagation direction.

$$\iint \mathbf{e}_n^\pm \times \mathbf{h}_m^\pm dS \mathbf{n} = 0 \quad \text{if } n \neq m \quad (37)$$

$$\iint \mathbf{e}_n^\pm \times \mathbf{h}_n^\pm dS \mathbf{n} = 1 \quad (38)$$

The radiated fields can be described by a summation of normal modes, as in Equation 39 and Equation 40. The coefficients of these modes are straightforward to calculate, due to Lorentz Reciprocity Theorem, if the waveguide's walls are perfectly conducting. Ideally, any higher order mode than the first TEM mode will be suppressed, and the calculation simplifies to $n = 0$. Additionally, it is assumed that the source is electrically small, which makes it possible to represent it with dipoles, further simplifying the equations [15].

$$\mathbf{E}^\pm = \sum_n a_n \mathbf{E}_n^\pm \quad (39)$$

$$\mathbf{H}^\pm = \sum_n a_n \mathbf{H}_n^\pm \quad (40)$$

Suppose a current source \mathbf{J}_1 excites a waveguide (as is the case with the dipoles in the TEM cell). Normally, such a current source would be driven with external fields, but for the sake of the argument, they are ignored. Only \mathbf{E} and \mathbf{H} are considered, which are the fields radiated by \mathbf{J}_1 . Additionally, \mathbf{E}_n^\pm and \mathbf{H}_n^\pm are the resulting waveguide fields, with the signs indicating the direction of propagation. Take Equation 27 and set $\mathbf{J}_2 = \mathbf{M}_1 = \mathbf{M}_2 = 0$. Now, only the current source \mathbf{J}_1 remains, and the Equation 41 emerges.

$$\oint_S (\mathbf{E}_n^\pm \times \mathbf{H} - \mathbf{E} \times \mathbf{H}_n^\pm) \cdot d\mathbf{S} = \iiint \mathbf{J}_1 \cdot \mathbf{E}_n^\pm dV \quad (41)$$

In case of the TEM cell, it is desirable that only the TEM mode is propagating, and that the source is represented by a dipole. When the expansions Equation 39, Equation 40 and the orthogonal property Equation 37 are used, and when considering an electric dipole, the Equation 42 arises. In this equation, the wave amplitudes a and b are given through the surface integral in the Lorentz Reciprocity theorem, with a being the wave going to the left side, and b to the other. The electric dipole moment \mathbf{m}_e is given by the current \mathbf{J} flowing through the infinitesimal wire. Note that only the electric field of TEM wave propagation is considered. In reality, more modes may propagate, for which the electric field must be replaced by the superposition of normal modes as in Equation 39.

$$\begin{pmatrix} a \\ b \end{pmatrix} = -\frac{1}{2}\mathbf{m}_e \cdot \mathbf{E}^\pm \quad (42)$$

$E_n^\pm?$

If this arbitrary current distribution forms an infinitesimal loop, the source can be represented by a magnetic dipole moment \mathbf{m}_m . It is defined by the product $\mathbf{m}_m = \mathbf{A} \cdot I$, an infinitesimal current loop with area A carrying a current I . This leads to Equation 43. This formulation assumes, that the magnetic field strength \mathbf{H}^\pm does not change over the loop area, i.e. the loop is electrically small. Otherwise, the magnetic field strength \mathbf{H}^\pm must be considered in the integration [6, 25].

$$\begin{aligned} \begin{pmatrix} a \\ b \end{pmatrix} &= -\oint_C \mathbf{E}^\pm dl \\ &= -\iint_{S_0} \nabla \times \mathbf{E}^\pm d\mathbf{S} \\ &= i\omega\mu_0 \iint_{S_0} \mathbf{H}^\pm \cdot d\mathbf{S} \\ &= i\omega\mu_0 \mathbf{m}_m \mathbf{H}^\pm \end{aligned} \quad (43)$$

If there are several modes propagating, it is useful to find the coefficients of the modes a_n and b_n in Equation 39 and Equation 40. In this case, the orthogonality property in Equation 37 is used to derive Equation 44a and Equation 44b [6]. The wire is described by a curve C , and the tangential vector $\boldsymbol{\tau}$ is used to integrate along this curve.

$$2a_n = -\int_C \boldsymbol{\tau} \cdot \mathbf{E}_n^- dl \quad (44a)$$

$$2b_n = \int_C \boldsymbol{\tau} \cdot \mathbf{E}_n^+ dl \quad (44b)$$

3.3.2 Modes in rectangular waveguides

A TEM cell is used for EMC test specifications. It makes the conduction of TEM waves possible, which resemble planar free-space waves. Additionally, it shields the waves from radiating to the sides, for which it has a clear advantage to a stripline [9, 13]. A simple

rectangular waveguide cannot be used for this application. Assuming that a monochromatic wave travels down the waveguide, the waves will propagate without dampening only at a certain angle of reflection on the perfectly conducting surface. A short mathematical proof can be shown here, using Maxwell's equation. It shows that the electric and magnetic fields in direction of propagation cannot both be zero.

$$\mathbf{E} = (E_{0,x} \cdot \mathbf{e}_x + E_{0,y} \cdot \mathbf{e}_y + E_{0,z} \cdot \mathbf{e}_z) e^{i(\omega t - kz)} \quad (45)$$

$$\mathbf{H} = (H_{0,x} \cdot \mathbf{e}_x + H_{0,y} \cdot \mathbf{e}_y + H_{0,z} \cdot \mathbf{e}_z) e^{i(\omega t - kz)} \quad (46)$$

$$\nabla \times \mathbf{E} = \begin{pmatrix} \frac{d}{dy} E_z - ik E_y \\ ik E_x - \frac{d}{dx} E_z \\ \frac{d}{dx} E_y - \frac{d}{dy} E_x \end{pmatrix} = \begin{pmatrix} -i\omega B_x \\ -i\omega B_y \\ -i\omega B_z \end{pmatrix} \quad (47)$$

$$\nabla \times \mathbf{B} = \begin{pmatrix} \frac{d}{dy} B_z - ik B_y \\ ik B_x - \frac{d}{dx} B_z \\ \frac{d}{dx} B_y - \frac{d}{dy} B_x \end{pmatrix} = \begin{pmatrix} \frac{i\omega}{\mu\epsilon} E_x \\ \frac{i\omega}{\mu\epsilon} E_y \\ \frac{i\omega}{\mu\epsilon} E_z \end{pmatrix} \quad (48)$$

If E_z and B_z , the fields in direction of propagation, were both zero, then the change of the transverse fields would be constantly zero, and because of the boundary conditions, all transverse fields would be zero. Equation 49 shows Gauss' law and Equation 50 Faraday's law if $E_z = B_z = 0$, from which the unchanging transverse electric field can be derived.

$$\frac{d}{dx} E_x + \frac{d}{dy} E_y = 0 \quad \text{Derived out of Gauss' law} \quad (49)$$

$$\frac{d}{dy} E_x - \frac{d}{dx} E_y = 0 \quad \text{Derived out of Faraday's law} \quad (50)$$

3.3.3 TEM Mode in TEM Cells

A TEM cell solves this problem, by having a gap between the septum and the side walls. Essentially, it can be considered as two rectangular waveguides with apertures on the sides. Those apertures allow perturbations of the electromagnetic fields between them. The boundary conditions of the Laplace equation now changed due to the gaps. The Green's function may be calculated of the new construction, now considering the boundary conditions at the gaps, which must be the same for both waveguides (to prevent discontinuities). In the papers of Tippet, Chang and Wilson, this new Green's function lead to the excitation of TEM modes in both waveguides [28, 30]. However, the gap is assumed to be small, electrically ($\xi g \ll 1$) and compared to the septum width ($g/a \ll 1$) [31]. The variable $\xi = \sqrt{k_0^2 - \beta^2}$ is the transverse (in y-direction) propagation constant, and consists of the free-space wave number k_0 and longitudinal (in z-direction) propagation constant β . The variables g and a are geometry variables of the TEM cell annotated in Figure 3.1.

To analyze the fields in a TEM cell, the dyadic Green's function discussed in subsubsection 3.2.2 proofs itself to be useful. It is assumed, that a vertical, electrically short antenna is inserted in the top center of the TEM cell. This is modeled by a current distribution in y-direction $\hat{\mathbf{J}}(\mathbf{x}) = \mathbf{a}_y J(\mathbf{x})$ [31]. Accordingly, the Green's function reduces to

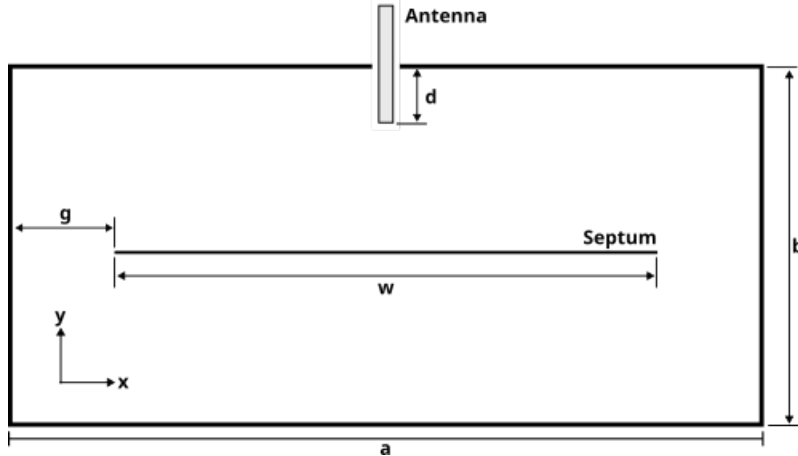


Figure 3.1 TEM cell with vertical antenna inserted

$\hat{\mathbf{G}}(\mathbf{x}, \mathbf{x}') = \mathbf{a}_y G(\mathbf{x}, \mathbf{x}')$. First, the Green's function for a rectangular waveguide $G_O(\mathbf{x}, \mathbf{x}')$ is shown in Equation 51 [2]. There, η_0 is the free-space impedance, $M = m\pi/(2a)$, $N = n\pi/b$ and $K_m = (\xi^2 - M^2)^{1/2}$. Furthermore,

$$\Delta_n = \begin{cases} \frac{1}{2}, & n = 0 \\ 1, & n > 0 \end{cases}$$

Check Vector notation. Is correct for Dyadics?

and,

$$g_{mn}(\mathbf{x}_t, \mathbf{x}'_t) = \left(\frac{2}{ab}\right) \sin M(x + a) \sin M(x' + a) \cdot \cos Ny \cos Ny'$$

are functions implemented in Equation 51. The components x , x' and y , y' are part of the vectors \mathbf{x}_t , \mathbf{x}'_t .

$$\tilde{G}_0(\mathbf{x}_t, \mathbf{x}'_t) = \frac{-j\eta_0}{k_0} \left\{ \sum_{m,n=0}^{\infty} \frac{\Delta_n[M^2 + \beta^2]}{M^2 + N^2 - \xi^2} g_{mn}(\mathbf{x}_t, \mathbf{x}'_t) \right\} \quad (51)$$

The TEM cells Green's function by adding a unperturbed term to it [31]. The derivation of those Green's Functions is demonstrated in [30], which uses the same methods described in [2], as mentioned above.

The perturbed term in Equation 52 describes the influence of the gaps on the field distribution. They are derived by forcing the tangential fields to be continuous across the gaps, then describing this boundary condition mathematically as a perturbing second Green's function. The rest of the boundary conditions on the are zero due to the geometry of the TEM cell. The functions used are,

$$L(\beta) = \left[\ln \left(\frac{8a}{\pi g} \right) - \frac{\pi}{a} \sum_{m \in \{1,3,5,\dots\}}^{\infty} \left(\frac{\cot K_m b}{K_m} + \frac{2a}{m\pi} \right) \right]^{-1}$$

and,

$$f(\mathbf{x}_t) = \sum_{m \in \{1, 3, 5, \dots\}}^{\infty} M \frac{\cos K_m(b - y)}{K_m \sin K_m b} \sin Ma \cos Mx J_0(Mg).$$

To receive the final Green's Function, the unperturbed and perturbed term are added together $G(\mathbf{x}_t, \mathbf{x}'_t) = G_O(\mathbf{x}_t, \mathbf{x}'_t) + G_g(\mathbf{x}_t, \mathbf{x}'_t)$. Naturally, the observation point \mathbf{x} can only be on the upper half in the chamber, where the source is also located [31].

$$\tilde{G}_g(\mathbf{x}_t, \mathbf{x}'_t) = \frac{-j\pi k_0 \eta_0}{2a^2 s^2} L(\beta) f(\mathbf{x}_t) f(\mathbf{x}'_t) \quad (52)$$

Because waves propagating in the TEM cell are assumed to travel into infinity, they might have any longitudinal propagation constant β . They are not limited by boundary conditions in this direction. It therefore proofs useful to apply a Fourier Series over this variable, as done in Equation 53. There, the subscript t indicates only the transverse (xy-plane).

$$G_O(\mathbf{x}, \mathbf{x}') = \frac{1}{2\pi} \int_{-\infty}^{\infty} \tilde{G}_0(\mathbf{x}_t, \mathbf{x}'_t) e^{j\beta z} d\beta \quad (53a)$$

$$G_g(\mathbf{x}, \mathbf{x}') = \frac{1}{2\pi} \int_{-\infty}^{\infty} \tilde{G}_g(\mathbf{x}_t, \mathbf{x}'_t) e^{j\beta z} d\beta \quad (53b)$$

This explanation is not directly cited but my interpretation. Make sure that this is correct info.

Now, the antenna impedance is calculated using the generic Equation 54. The Green's Function in this represents the electric field excited by an unit strength dipole [31]. Scaled by multiplication with the current density $\mathbf{J}(\mathbf{x})$ and integrated over the length of the wire, results in the total electric field. Next, by multiplying it by the current distribution $\mathbf{J}(\mathbf{x})$ and integrated over the length of the wire again, leads to the apparent power. In the end, dividing this term by the total current consumption squared I^2 leads to the impedance.

$$Z = \frac{-1}{I^2} \int_S \int_{S'} \mathbf{J}(\mathbf{x}) \cdot \mathbf{G}(\mathbf{x}, \mathbf{x}') \cdot \mathbf{J}(\mathbf{x}') ds' ds \quad (54)$$

When evaluating the real part of the impedance for the case described here, the radiation resistance results from Equation 55. If the inserted antenna is electrically small, as it is in this case, d reduces the influence of other terms. The most dominant term then, k_0^2 , results in a quadratic relation of the radiation resistance to the frequency. This agrees with the theoretical framework in the discussion about small dipoles in ??, as well as with the simulations results in section 4.

$$R = \frac{\pi \eta_0 k_0^2}{4a^2} \csc^2 k_0 d L(k_0) H(k_0) \quad (55)$$

Here,

$$H(\beta) = \sum_{m' \in \{1, 3, 5, \dots\}}^{\infty} h_{m'}(\beta) \sum_{m \in \{1, 3, 5, \dots\}}^{\infty} h_m(\beta) J_0(r(M^2 + \beta^2)^{1/2})$$

and,

$$h_m(\beta) = \frac{M \sin Ma J_0(Mg)}{K_m \sin K_m b} \cdot \frac{\cos k_0 d - \cos K_m d}{M^2 + \beta^2}.$$

Give a short interpretation of each variable. Subdivide the text into subsections

3.3.4 Higher order modes in TEM cells

The TEM cell used in the simulation has a width of $a = 40$ mm and a height of $b = 24$ mm. A cross section of the TEM cell with the important dimensions is shown in Figure 3.2. The cutoff frequencies of the higher order TE and TM modes can be approximated by the same formula, shown in Equation 56 for rectangular waveguides. However, this is only true, if the septum is very thin ($t/b \ll 0.1$), and for modes with n-even subscripts, i.e. $\text{TE}_{m,2n}$ and $\text{TM}_{m,2n}$ modes.

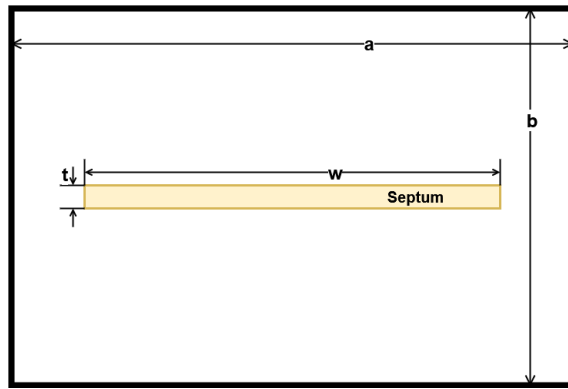


Figure 3.2 Cross section of the TEM cell

$$f_c = \frac{c}{2} \sqrt{\left(\frac{m}{a}\right)^2 + \left(\frac{n}{b}\right)^2} \quad (56)$$

- f_c : cutoff frequency of the mode T_{mn}
- c : speed of light in the medium (approximately 3×10^8 m/s in air)
- a : wider dimension (broad wall) of the rectangular waveguide (meters)
- b : narrower dimension (narrow wall) of the rectangular waveguide (meters)
- m : mode index in the a -direction (integer, $m \geq 0$)
- n : mode index in the b -direction (integer, $n \geq 0$)

The cutoff frequency of the TE_{10} mode is around 3.75 GHz, according to Equation 56. To verify this, a modal analysis was performed in Ansys HFSS, where an empty TEM cell was modeled with two waveports defined at its output. The resulting S_{12} -parameters are presented in Figure 3.3. The black line shows the S_{12} -parameter over the frequency of the TEM mode, while the blue line demonstrates S_{12} -parameter of the TE_{10} mode. At a frequency of 3.75 GHz, the mode propagates without attenuation, where the cutoff frequency $f_{c,10}$ is defined. The simulated result comes very close to the analytically determined one.

The red trace shows a cutoff frequency of $f_{c,01} = 3.12 GHz for the TE_{01} mode. Equation 56 would predict a cutoff frequency of 6.25 GHz, however, the septum influences n-odd modes like this one. Their cutoff frequencies are shifted to a lower value [29].$

The frequency in simulations with the TEM cell will range from 1 MHz to 3 GHz. This guarantees that the higher order modes will not influence the simulation results.

In a real TEM cell, a tapered section transform the TEM waveguide to a coaxial transmission line. This section does not cause reflections of waves in TEM mode. However, higher order TE and TM modes get reflected, and because the TEM cell is a high-Q cavity, resonances occur at $\frac{\lambda}{4}$ or $\frac{\lambda}{2}$ [13]. This is not considered in these simulations, since the simulation model does not contain this tapered section.

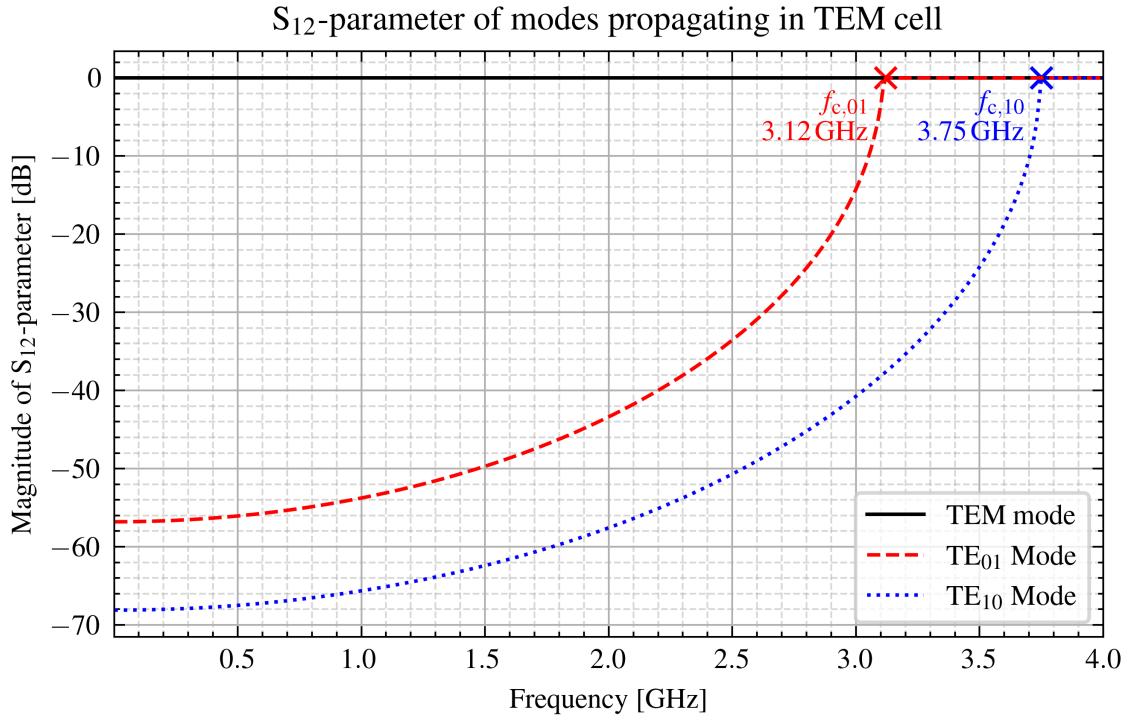


Figure 3.3 Propagation of TEM, TE_{01} and TE_{10} modes in TEM cell

The TEM cell does not only support TEM modes, above their cut-off frequency TE and TM modes begin to propagate. Because the TEM cell is a high-Q cavity, those cut-off frequencies are sharply defined frequencies. Due to imperfections, change in materials or finite conductivity of the conducting plates, wave propagating in the TEM mode may excite

higher order TE and TM modes, too [14]. A change in material, for example, demands the electric and magnetic field to have a component in the direction of propagation at the discontinuity. A paper by Wilson and Ma present analytical approximations to determine these frequencies [33]. There is a long list for the several first few corner frequencies of the first modes. Additionally, a paper by Koch, Groh and Garbe determines the resonance frequencies of the first TE modes analytically [14]. The TEM mode is necessarily excited by the geometry of the TEM cell, hence this mode is called essential. The higher order TE and TM modes, which are only excited due to non-uniformity of the TEM cell, are called non-essential modes [13].

The first modes propagating after the TEM mode is the TE₁₀ and TE₀₁ modes. Their transversal electric fields are depicted in Figure 3.4.

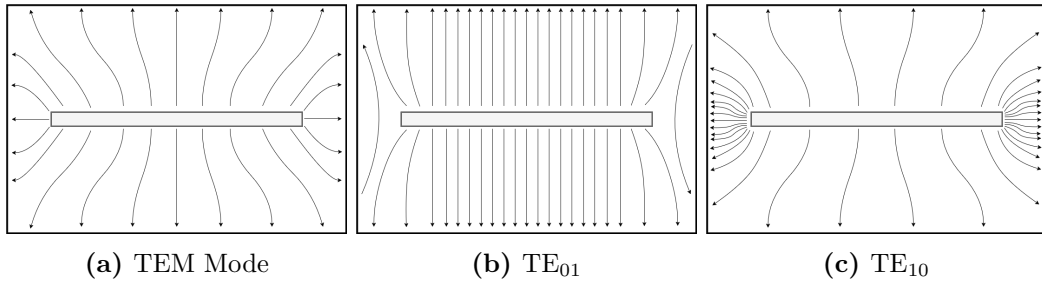


Figure 3.4 Transversal electric fields in cross section of TEM cell

The cut-off frequencies are dependent on the dimensions of the TEM cell, as previously shown. Table 1 shows some cut-off frequencies of these modes for different TEM cell dimensions. The TE₁₀-mode is independent of the height b of the TEM cell, as would be the case in a rectangular waveguide. Both the TE₁₀-mode and the TE₀₁-mode are dependent on the width a . Note that a port impedance of 50Ω is only kept in the case $a = 40\text{ mm}$ and $b = 24\text{ mm}$. This information is important when varying the TEM cell dimension, as is done when investigating near-field ($k \cdot r < 1$) and intermediate-field ($k \cdot r = 1$) coupling.

Vector directions are wrong in the pictures. Additionally, update cutoff frequencies.

Table 1 Cut-off frequencies of higher order modes depending on TEM cell dimensions

a [mm]	b [mm]	TE ₀₁ f_c [GHz]	TE ₁₀ f_c [GHz]
80	24	1.89	2.05
40	24	3.17	3.76
40	48	2.10	3.76

3.4 Electrically Small Radiating Sources in TEM Cells

An electrically small radiating source may be represented by six dipoles. This number includes three magnetic dipoles pointing in every direction of the Cartesian coordinate system (x, y, and z-direction), and three electric dipoles in the same orientation. Consequently, an equipment under test (EUT) could be modeled with these dipoles, leading to much less computational effort in simulation. The excited EM waves by point sources is

discussed in [6] and in subsection 3.3. An analytical procedure to determine these dipole moments is presented by Sreenivasiah [25], and some experimental results based on it can be found in the research of Kreindl, where bond wires were modeled with magnetic dipoles[16], and, again, Sreenivasiah [25].

The idea is to place the EUT in the TEM cell and measure the power of both output ports. The amplitudes of the TEM fields are expressed by Equation 57 [25].

$$\begin{pmatrix} a \\ b \end{pmatrix} = \frac{1}{2}(-\mathbf{m}_e \cdot \mathbf{E}_0^\pm + i\omega\mu_0\mathbf{m}_m \cdot \mathbf{H}_0^\pm) \quad (57)$$

The magnetic field \mathbf{H}_0 and electric field \mathbf{E}_0 are both normalized to $1\sqrt{\text{Hz}}$ [16] and correspond to the TEM mode in free space [25]. The electric dipole moment \mathbf{m}_e and the magnetic dipole moment \mathbf{m}_m are complex vectors, containing an amplitude and phase for every one of the three directions in the coordinate system (x, y, z), and have the units $\text{A} \cdot \text{m}$ and $\text{V} \cdot \text{m}$. The variables a and b correspond to the amplitudes of the waves in both possible directions in the TEM cell with the unit $\sqrt{\text{W}}$. This leads to the final form in Equation 58 [25].

$$\begin{pmatrix} a \\ b \end{pmatrix} = -\frac{1}{2}(\mathbf{m}_e \pm i\mathbf{k}\mathbf{m}_m \times \mathbf{z}) \cdot \mathbf{e}_0 \quad (58)$$

The unity vector \mathbf{z} points in direction of propagation. The function vector \mathbf{e}_0 describes the normalized electric field amplitude in traverse direction, i.e. x and y-directions, of the excited fundamental mode. Due to the normalization of the electric and magnetic fields to $1\sqrt{\text{W}}$, the total power at one port is 1 W. This defines \mathbf{e}_0 as the electric field when the TEM cell is excited with a peak unit power, since the amplitude of the electric field is considered, not the RMS value.

Note, that an electric dipole in the TEM cell leads to a increase in power with the same phase in both ports, and a magnetic dipole leads to the same increase, but with a phase shift of 180° . This also explains why the EUT shall be place halfway on the septum in x-direction. Any shift from this position changes this phase shift from 180° . It is therefore required to measure the power of the ports with phase information, like using a complex Poynting vector, which is easy to implement in a simulation software. When measuring a device with a real TEM cell, the phase information may be found by summing and subtracting the output powers of the ports, as is shown in [25].

peak
power,
not av-
erage.
Explain
better.

Additionally, only the electric or magnetic dipole moment, that is aligned with the electric or magnetic field in the TEM cell, influences the output power, ideally. Furthermore, in the optimal case, the EUT is placed in the dead center of the TEM cell, where the x- and z-component of \mathbf{e}_0 in the $y=0$ plane becomes zero due to symmetry [25]. If this is not the case, the measurements may vary significantly [17].

The formula has originally been derived for cylindrical waveguides [6]. There, the position of the electric and magnetic dipole moments do not matter, as long as the matching electric and magnetic fields at the surfaces are chosen. This is because the field components

do not change direction when propagating from the dipoles to the surfaces, due to the symmetrical property of the cylindrical waveguide. This is not the case for a TEM cell. There, an offset into the x- and y-direction from the center leads to field components, which change direction while traveling to the surfaces. Then, the vector product used in the derivation by Lorentz Reciprocity theorem is not valid anymore. Instead, the fields at the test points have to be considered, and because they don't have a singular x,y or z-component anymore, several more dipole moments become relevant.

This analysis might be wrong. The normalized E-Field is something different here than previously - I mixed it up. What could work: Simulate electric dipole moment in y-direction with geometry sweep. Adjust y_0 in [25]. Find norm. E-Field for that. Simulate output power. Compare with calculations.

However, in a TEM cell, the normalized electric field strength is not necessarily symmetrical. Therefore, it must be found out, depending on the position of the dipole moment. In dead center, the normalized electric field only has a z-component. However, with an offset towards z- or y-direction, it will have a y-component, too. Then, the normalized electric field \mathbf{e}_0 can be found with through Equation 59a for and Equation 59b. For these equations, a known electric dipole moment m_{se} is used for both the x- and z-direction. P_x and P_z describe the output powers at one port, depending on the electric dipole's orientation [25]. When knowing the normalized electric field \mathbf{e}_0 at this point, any magnitude of electric dipole moments may be derived by scaling the coefficients a and b . When only considering dipole moments in z-direction, then only Equation 59b is needed.

$$e_{0x} = \frac{2\sqrt{P_x}}{m_{se}} \quad (59a)$$

$$e_{0z} = \frac{2\sqrt{P_z}}{m_{se}} \quad (59b)$$

The normalized electric field of the TEM mode is then given by Equation 60a in x-direction and by Equation 60b in z-direction [33]. The equations follow from the singular integral-equation approach in [30]. The formula is not valid for the gap regions. However, since there won't be any dipole moment placed there, this approximation will suffice. These equations are to understand the influence of electrically small structures, which do not align with the TEM modes, but still couple with the TEM cell and influence the results.

$$e_{ox} = \frac{2}{a} Z_c^{1/2} \sum_{m_0=1}^{\infty} \frac{\sinh M(b-pz)}{\sinh Mb} \cdot \sin Mx \sin Ma J_0(Mg) \quad (60a)$$

$$e_{oz} = p \frac{2}{a} Z_c^{1/2} \sum_{m_0=1}^{\infty} \frac{\cosh M(b-pz)}{\sinh Mb} \cdot \cos Mx \sin Ma J_0(Mg) \quad (60b)$$

Z_c is the characteristic wave impedance, a is half the width of the TEM cell, b is half its height. The sign-function $p = 1$ above the septum, and $p = -1$ below it. $M = m\pi/2a$

Is the series for several sine-waves fitting into the TEM cell, derived due to the nature of the Green's Function? If yes, then only the

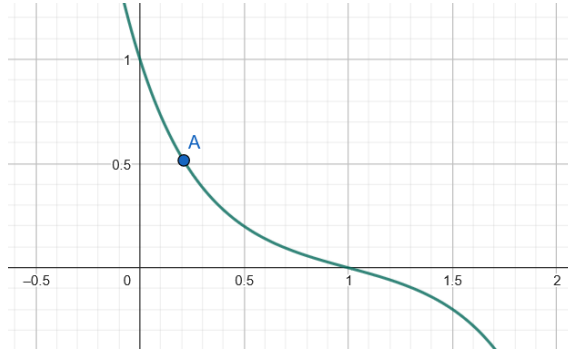


Figure 3.5 Normalized e-field distribution along z-axis at center of septum for visualization, where the y-axis is the magnitude and the x-axis is the point in the height position in the TEM cell.

$$E_{ox} = \frac{2}{a} Z_c^{1/2} \sum_{m=1}^{\infty} \frac{\sinh M(b-py)}{\sinh Mb} \cdot \sin Mx \sin Ma J_0(Mg)$$

$$E_{oy} = p \frac{2}{a} Z_c^{1/2} \sum_{m=1}^{\infty} \frac{\cosh M(b-py)}{\sinh Mb} \cdot \cos Mx \sin Ma J_0(Mg)$$

Figure 3.6 TODO: This is how the dimensions in these formulas are defined in [30]

and g is the length of the gap between the septum and the conducting wall. The index $m = 1, 3, 5, \dots$ is iterated over odd integers.

The normalized electric field intensity may be derived by the numerically resulting output power when placing dipole moments in the TEM cell. For example, Figure 3.7 demonstrates the output power of an electric dipole moment in the y-direction. It is shifted in the y-direction at center height between septum and upper TEM cell wall. Applying Equation 59a to the output power leads to the normalized magnitude of the field intensity in y-direction e_y . The distribution follows that of the magnitude of a sine wave, according to Equation 60a. There, at $y = 0$ mm, the normalized electric field strength equals zero, and approaches a maximum at $y = \pm 20$ mm. However, since this equation is valid outside the gap region, and the gap region is not relevant for further research, the is limited at an offset of $y = \pm 15$ mm.

Furthermore, ?? demonstrates the output power and the normalized e_y -field across the height from the septum to the upper TEM cell wall. The dipole moment is subject to an offset of $y = 7.5$ mm from the center. That is because the output power and normalized electric field strength is constantly zero at $y = 0$ mm, independent of the height.

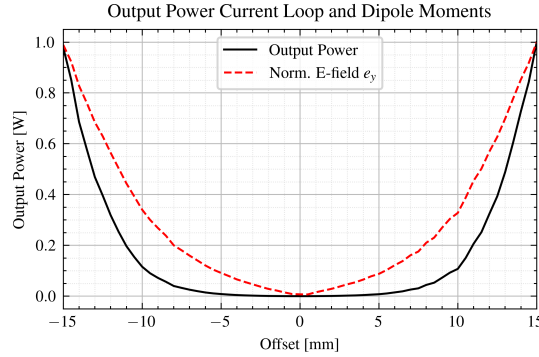


Figure 3.7 Output power and norm. E-field over offset

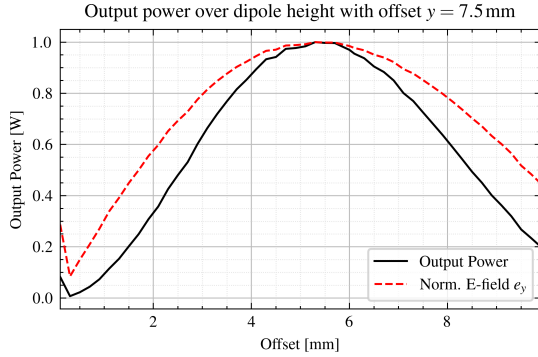


Figure 3.8 Output power and norm. E-field over height

3.5 Shielding

Effective shielding is of great interest to reduce EMI of electronic systems. A figure of merit for shielding capabilities of a material is the electromagnetic shielding effectiveness (SE), given in Equation 61 [7]. E_i is the incident electric field, while E_t is the transmitted electric field, also depicted in Figure 3.9. It depends on the thickness and shape of the material, and its electric and magnetic properties. Additionally, the TEM cell contributes to the SE values.

$$SE_{dB} = 20 \log \left(\frac{E_i}{E_t} \right) \quad (61)$$

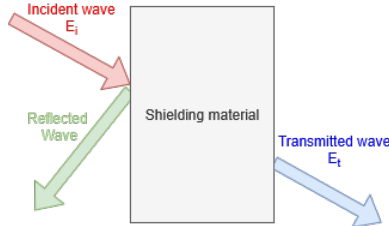


Figure 3.9 Incident, reflected and transmitted electric fields due to interaction with shielding material

An electromagnetic wave may undergo several reflections inside the shielding material, with each reflection adding up to the total reflected, absorbed and transmitted waves. The total shielding effectiveness is therefore determined by Equation 62, according to Schelkunoff. A_{dB} represents the absorption losses traveling through the shield, R_{dB} the reflection losses, and B_{dB} is the correction factor for the multiple reflections inside the shield [7].

$$SE_{dB} = R_{dB} + A_{dB} + B_{dB} \quad (62)$$

Calculate with S-params S_{11} and S_{21} : A, R and T.

This approach to shielding with internal re-reflections in the shielding material was derived by Schelkunoff. https://www.ieee.li/pdf/viewgraphs/fundamentals_electromagnetic_shield.pdf

The reflections occur due to the change in wave impedance. They are described through a reflection coefficient R . Additionally, it is common to normalize the wave impedance Z to the free-space wave impedance Z_0 . At the interface from free-space to a shielding material, this leads to Equation 63 [6].

$$R = \frac{Z - 1}{Z + 1} \quad (63)$$

$$Z = \frac{1}{Z_0} \sqrt{\frac{i\omega\mu}{\sigma + i\omega\epsilon}} \quad (64)$$

The reflection coefficient can be converted into dB, leading to R_{dB} . Any additional reflection happen due to re-reflections inside the shielding material, described by B_{dB} . The rest of the energy must either be absorbed, described by A_{dB} or transmitted, shown by T_{dB} .

The wave number k in lossy media is described in a real and imaginary parts as in Equation 65. The imaginary part α is the attenuation or absorption coefficient. It describes the reduction of the intensity of the wave, which occurs with $e^{-\alpha x}$, where x is the coordinate direction of propagation. The real part $\beta = \frac{2\pi}{\lambda}$ is the phase constant [12].

$$k = \beta + i\frac{\alpha}{2} \quad (65)$$

$$\mathbf{E} = \mathbf{e} \cdot e^{ikx} \quad (66)$$

When the molecules in a material are exposed to electric fields, they will polarize, described by their permittivity ϵ . When exposed to a magnetic field, the spinning of their electrons in the atoms align with the magnetic field, described by the permeability μ of the material. When the fields alternate over time, the molecules will always move and align according to them. This is essentially a movement of charges, and therefore described by a conductivity σ . The energy lost in this process is dissipated as heat [1].

The electric field will push charges in polarizable molecules apart. This separation of charges may be described as an electric dipole, depending on the separation distance and the charge. Under alternating electric fields, the moving of charges will contribute to σ . This phenomenon is called dielectric hysteresis. Equation 67 quantifies it by a loss tangent $\tan \delta_e$ [1]. There, σ_s is the static conductivity, meaning the conductivity of the material for static fields. The complex part of the permittivity ϵ'' describes the lossy part of the dielectric material, specifically relevant for the alternating fields case. The real part of the permittivity is lossless and is noted by ϵ' . The overall complex permittivity is therefore $\epsilon = \epsilon' + i\epsilon''$.

$$\tan \delta_e = \frac{\sigma_s}{\omega\epsilon'} + \frac{\epsilon''}{\epsilon'} \quad (67)$$

p. 309
Classical
Electrodynamics
(John
David
Jackson)
describe
shielding
material
by dipole
moments

Formula
 α ?
Needed?

S-
parameters
should
enable
derivation
of α . Due
to normal
incident
wave of
TEM,
no angle
needed to
consider.

Basics:
Balanis
2012 page
68?

The loss tangent therefore $\tan \delta_e$ relates the conductivity of a material to the real permittivity. A dielectric with low losses has a much larger displacement current than conduction current density ($\tan \delta_e \ll 1$). The opposite is true for a good conductor ($\tan \delta_e \gg 1$) [1].

The loss tangent $\tan \delta_e$ is a function of frequency, however, it is often not stated as such. Therefore, the loss tangent of FR4, for example, is given as $\tan \delta_e = 0.02$ for frequencies up to 1 GHz. For higher frequencies, the molecules may have resonance frequencies, where they influence more strongly the overall conductance and consequently increase the imaginary part of the permittivity ϵ'' .

There are also magnetically lossy materials, which is introduced by a complex permeability $\mu = \mu' + i\mu''$. Analog to the dielectric case, the permeability can also be described by a loss tangent $\tan \delta_m$ as shown in Equation 68. However, the loss tangent is very low for the majority of materials and will be neglected. Ferrites are an exception, which are commonly used to dampen high frequency signals [1].

$$\tan \delta_m = \frac{\mu''}{\mu'} \quad (68)$$

Electric fields dominate in the near-field region of electric dipoles. To shield them, high permittivity and high conductivity materials, ideally with a high loss tangent $\tan \delta_e$ shall be used. On the other hand, magnetic fields dominate in the near-field region of magnetic dipoles. For shielding them, high permittivity and high conductivity materials, again with a high loss tangent $\tan \delta_m$ shall be used.

describe
 α and δ
for ab-
sorption.
Then re-
flections
with ϵ
and μ
source

3.5.1 ASTM ES7-83 Method

The ASTM ES7-83 method is used to determine the shielding effectiveness of shielding materials. The shielding material is inserted into a coaxial TEM cell around the septum. Ideally, they form a continuous connection [23].

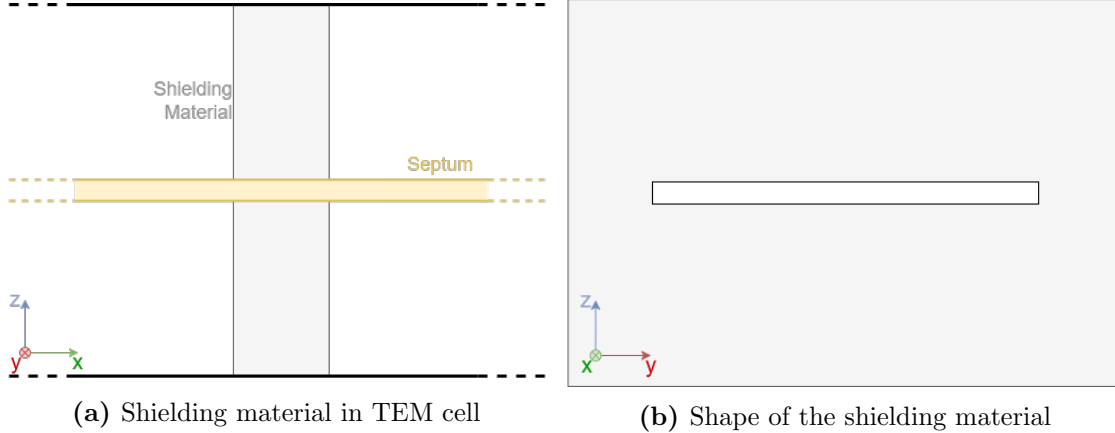
In this method, two measurements are performed with an oscilloscope attached to the output of the TEM cell. In the first, an empty TEM cell is excited and a reference output voltage U_{ref} is measured. In the second, the TEM cell is loaded with the shielding material, and the output voltage U_{load} is again noted. The measurement values are then used in Equation 69 to derive the shielding effectiveness SE_{dB} [23].

$$SE_{\text{dB}} = 20 \cdot \log \left(\frac{U_{\text{ref}}}{U_{\text{load}}} \right) \quad (69)$$

In the case of simulating the problem, such a procedure may be used, too. It is more convenient, then, to define a reference output power P_{ref} for an unloaded TEM cell, and a output power for the loaded case P_{load} . This leads to the similar Equation 70.

$$SE_{\text{dB}} = 10 \cdot \log \left(\frac{P_{\text{ref}}}{P_{\text{load}}} \right) \quad (70)$$

Additionally, a rectangular TEM cell is used for this method, instead of the commonly used cylindrical version. Figure 3.10b shows the cross section of this shielding material, which is inserted into the TEM cell. In Figure 3.10a the shielding material can be seen wrapped around the septum.



Then, the S-parameters derived in the simulations are used to get to the output powers P_{ref} and P_{load} . By exciting the TEM cell with a power of 1 W, the reference power $P_{\text{ref}} = 1 \text{ W}$. The measured power is then derived through Equation 71.

$$P_{\text{load}} = P_{\text{ref}} \cdot 10^{|S_{12}|/10} \quad (71)$$

3.5.2 Dual TEM cell

The shielding effectiveness of a material may also be determined using two TEM cells, which are stacked upon each other, as shown in Figure 3.11. They are connected through an aperture, which can be filled with the shielding material. One TEM cell is excited, and therefore acts as a driving cell. It transmits power through the aperture. It is measured at the second TEM cell, which acts as a receiver. The dual TEM cell simulates near-field conditions, opposed to the far-field conditions simulated by the simple TEM cell [23]. This is important when using the shielding material to shield an antenna's radiation by placing the material directly next to it.

The electrically small aperture may be described by an electric and a magnetic dipole moment. Their magnitude is related to the electric and magnetic coupling between the TEM cells over the aperture. Therefore, the electric and magnetic coupling can be determined separately by adding or subtracting the output powers of the receiving TEM cell [23, 32]. Consequently, an electric shielding effectiveness SE_{dB}^e can be calculated with Equation 72a, and a magnetic shielding effectiveness SE_{dB}^m with Equation 72b. If a material, for example, permits energy transfer because of magnetic dipoles in it, then a measurement with lower SE_{dB}^m than SE_{dB}^e is to be expected [32].

Describe Method.
Then follows dual TEM cells

must it be electrically small?

$$SE_{\text{dB}}^e = 10 \log \left(\frac{P_{\text{ref,sum}}}{P_{\text{load,sum}}} \right) \quad (72a)$$

$$SE_{\text{dB}}^{\text{m}} = 10 \log \left(\frac{P_{\text{ref,diff}}}{P_{\text{load,diff}}} \right) \quad (72\text{b})$$

Because the normalized electric field at the aperture will be of TEM mode, only the component normal to the aperture in z-direction has to be considered. Just as in the case of dipole representation, the Lorentz Reciprocity theorem may be applied to find the fields in the TEM cell. Because both the fields at the output and in the aperture are of TEM mode, only the E-field at the output may be considered.

Since the aperture is electrically small, the field quantities may be assumed to be constant over it. This makes it possible to represent the energy transfer by dipole moments.

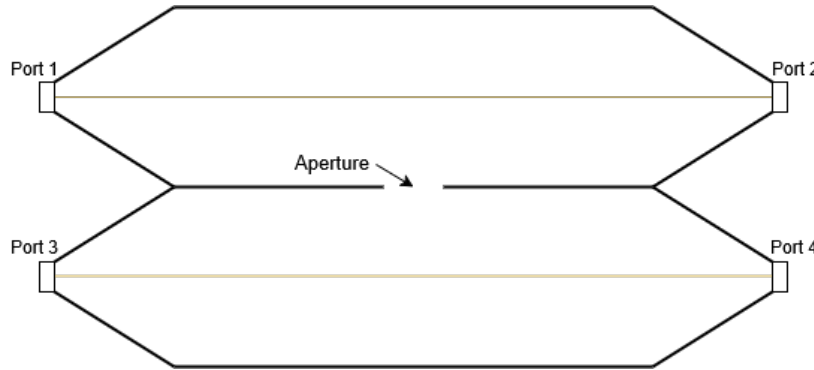


Figure 3.11 Dual TEM cell with aperture

4 Numerical Investigations

4.1 Finite Element Method

4.1.1 General Idea

Problems involving the calculations of electromagnetic fields are often cumbersome and difficult to solve. This is due to the need of solving differential equations describing these fields over a computational domain, which is not possible with a computer in this sense. The simulation software Ansys HFSS (High Frequency Simulation Software) aims to provide a solution. This software is used for the simulations in section 4, hence it is described in this following, dedicated section.

HFSS uses a numerical technique, namely the Finite Element Method (FEM). The general idea of FEM after Rayleigh-Ritz-Galerkin is to choose a number of basis functions. The goal is to find a linear combination of these basis functions, so that the differential equation is satisfied as closely as possible. This turns the problem of solving a differential equation into a system of algebraic equations, which the computer can process. There is always a set of basis functions which enable the calculation to converge to the real solution. However, the number of basis functions used in the domain is limited, due to reasons of computability [26].

FEM therefore divides the domain into finite elements, i.e. smaller pieces. Then, within each piece, such a basis function is assigned. A linear combination of these basis functions

are found, which satisfy the differential equations. In region where the approximating solution has a high degree of error, the accuracy may be increased by further subdividing the finite elements. This is repeated, until the error falls below a certain threshold, and a precise solution is derived.

4.1.2 Dividing a computational domain into finite elements

The differential equation to be solved is shown in Equation 73, where ϵ_r is the relative permeability and μ_r is the relative permeability of the material. The variable k_0 is the wave number of free space and equals $k_0 = \omega\sqrt{\epsilon_0\mu_0}$. [5, 19, 4].

$$\nabla \times \left(\frac{1}{\mu_r} \nabla \times \mathbf{E} \right) - k_0^2 \epsilon_r \mathbf{E} = 0 \quad \text{in } \Omega \quad (73)$$

This equation is solved in a computational domain Ω . This computational domain is divided into finite elements, called a mesh. Each node in this mesh has polynomial functions assigned, which are weighted to approximate the real solution. It has been proven that tetrahedral finite elements are best suited for this task, as they are geometrically flexible and make the definition of complete polynomial approximation functions possible [24]. Ansys HFSS uses a adaptive finite element mesh generator, which automatically provides a mesh for a given 3-dimensional construction. The Delaunay tessellation for three-dimensions is used for generating a mesh. It efficiently creates a mesh from objects of arbitrary shapes. Any boundary condition can be added recursively to the mesh. At the heart of this algorithm lies the property, that the circumsphere of an tetrahedra's vertices may not contain other tetrahedra's vertices.

Figure 4.1 shows one of such tetrahedrons. At the edge points, the components of the field which are normal to the respective edge and tangential to the face of the element is stored. At the vertex points, the component of a field which are tangential to the edges are stored. The value of the field at any midpoint is derived through interpolation from the node values. The basis function is used for interpolation.

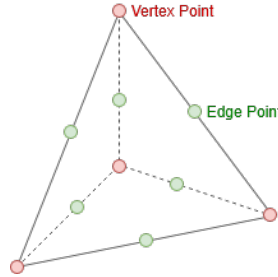


Figure 4.1 Tetrahedron with points on the edge and vertices.

Because of the way how the fields are stored in the tetrahedra, they are called tangential vector finite elements. Their advantage is that tangential components of fields can be forced to be equal among adjacent tetrahedra at the boundary. For example, an electric field stored at a vertex point must point in the direction along one of the edges, therefore it

is tangential to the element. An adjacent element then has the same tangential electric field imposed at this node, leading to a continuous tangential electric field, therefore satisfying the boundary conditions implied by the Maxwell equation automatically. Furthermore, any Dirichlet boundary conditions can easily be set along the edges. [19].

The finite element is described as Equation 74, where $L_2(\Omega)$ is a set of square integrable functions and P_1 a set of piecewise linear functions in the discretized domain Ω [20]. The vector fields at the vertices are given as u . $D(\Omega)$ is a set of divergence free functions. The vectors u used in the finite element therefore

- are continuous in the normal direction.
- are square integrable.
- have a curl describable by piecewise linear functions.

$$H_1^{(\text{dim}=3)}(\text{curl}) = \left\{ \mathbf{u} \mid \mathbf{u} \in [L_2(\Omega)]^3, \nabla \times \mathbf{u} \in [P_1(\Omega)]^3 \cap D(\Omega) \right\} \quad (74)$$

Figure 4.2 shows the finite element with the unknowns marked at each point. For reasons of simplicity, only the face is shown. The variables u_i^j and u_j^i are imposed across element boundaries, therefore guaranteeing tangential continuity at boundaries. Additionally, they inherently defined a linear polynomial, meaning that they describe a gradient of the field along this edge. Equation 75 describes this relation mathematically, where \mathbf{t}_{ij} is the unit vector tangentially to the edge from node i to node j and l_{ij} is the length of this edge.

$$\mathbf{u} \cdot \mathbf{t}_{ij} = \frac{1}{l_{ij}} (u_i^j - u_j^i) \quad (75)$$

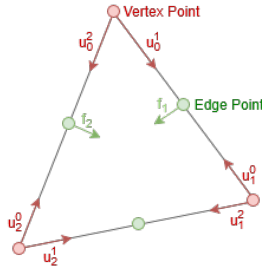


Figure 4.2 Face of the finite element with unknowns

Two facial unknowns f_1 and f_2 are added to two of the three edge points at one face. Contrary to the variables u_i^j , the facial unknowns f_i are only assigned locally at each element and do not cross boundaries. The purpose of the facial unknowns f is to provide a quadratic polynomial for the field component normal to the edges. This will lead to a linear approximation for the curl of the unknown vector field $\nabla \times \mathbf{u}$, providing sufficient accuracy. The overall vector field of this element is then calculated by a superposition of all nodes' vector attributions.

4.1.3 Solving the differential equation

A testing function \mathbf{W}_n is defined, which is multiplied to Equation 73. Integrating over the whole test volume then leads to Equation 76. This yields N equations, with $n = 1, 2, \dots, N$, for each finite element in the domain Ω . This is a common procedure in FEM, and it works through orthogonalization of the residual of Equation 73 with respect to the function \mathbf{W}_n . This means the new goal of the solution is to minimize the residual by making \mathbf{W}_n as orthogonal as possible [22].

$$\int_{\Omega} \left(\mathbf{W}_n \cdot \nabla \times \left(\frac{1}{\mu_r} \nabla \times \mathbf{E} \right) - k_0^2 \epsilon_r \mathbf{W}_n \cdot \mathbf{E} \right) dV = 0 \quad (76)$$

Using the vector identity $\nabla \cdot (\mathbf{a} \times \mathbf{b}) = (\nabla \times \mathbf{a}) \cdot \mathbf{b} - \mathbf{a} \cdot (\nabla \times \mathbf{b})$ on Equation 76 provides a weak form of the equation, meaning a form of the original partial differential equation, which does not contain all original derivatives [5, 4]. Additionally, boundary terms come into play, as seen in the right hand side of the resulting Equation 77. The usefulness in this step has been described as lowering the highest-order derivative, therefore the approximating functions need to guarantee continuity of value, not of slope [11]. Another explanation is the possibility of incorporation of Neumann boundary conditions [22].

$$\int_{\Omega} \left[(\nabla \times \mathbf{W}_n) \cdot \frac{1}{\mu_r} \nabla \times \mathbf{E} - k_0^2 \epsilon_r \mathbf{W}_n \cdot \mathbf{E} \right] dV = \underbrace{\oint_{\partial\Omega} \left(\mathbf{W}_n \times \frac{1}{\mu_r} \nabla \times \mathbf{E} \right) \cdot d\mathbf{S}}_{\text{Boundary term}} \quad (77)$$

Next, the electric field \mathbf{E} is represented by a superposition of basis functions. When applying Galerkin's method, the basis functions are equal to the test functions W_n . Equation 78 demonstrates the sum of the basis functions, which are weighted with the variable x_m . These variables x for all elements have to be solved, to find the electric field \mathbf{E} over the whole domain. The FEM has therefore reduced the initial wave equation in Equation 73 to a simple linear matrix equation $Ax = b$, where A is a known $N \times N$ matrix, b contains port excitations and x is the unknown. Ideally, the basis functions are defined to be zero outside of their adjacent elements. This will result to zero for all entries in the matrix, where the test and basis function do not overlap. Therefore, the matrix is sparse, and will be solved much faster. In the end, other electromagnetic quantities can all be derived through the electric field.

$$\mathbf{E} = \sum_m^N x_m \mathbf{W}_n \quad (78)$$

Equation 79 shows what the matrix then looks like. Some manipulation on the boundary term have been made, so that it contains the surface impedance Z_s . The surface impedance defines the ratio of the electric field to the magnetic field on the boundary region. Furthermore, it contains the free space, which equals $\eta_0 \approx 377 \Omega$.

$$A_{ij} = \int_{\Omega} \nabla \times \mathbf{W}_i \frac{1}{\mu_r} \nabla \times \mathbf{W}_j dV - k_0^2 \int_{\Omega} \mathbf{W}_i \epsilon_r \mathbf{W}_j dV + ik_0 \left(\frac{\eta_0}{Z_s} \right) \oint_{\partial\Omega} \mathbf{n} \times \mathbf{W}_i \cdot \mathbf{n} \times \mathbf{W}_j dS \quad (79)$$

4.1.4 Adaptive solution process

Each finite element therefore has a solved electric field assigned, which should approximate the real solution as closely as possible. To determine the error for each element, Equation 73 is evaluated. The elements with the highest residuals contain the largest deviation from the real result, meaning they have a large degree of error. Region in the mesh with large degrees of errors are refined, i.e. the tetrahedral finite elements are split into smaller ones. This allows the FEM solver to recalculate the fields in this region with higher precision, leading to a smaller residual. Consequently, the finite elements represent the fields more accurately, due to a smaller element size and higher resolution [3]. An additional method is increasing the order of the polynomial basis functions of elements with low degree of accuracy.

$$\nabla \times \left(\frac{1}{\mu_r} \nabla \times \mathbf{E}_{\text{solved}} \right) - k_0^2 \epsilon_r \mathbf{E}_{\text{solved}} = \text{residual} \quad (80)$$

To determine when the iterative refinement process is done and the solution good enough, some kind of threshold must be defined. One possibility is the Max ΔS parameter. It is compared to the difference of S-parameters of the defined excitation ports over two iterations. If, after a mesh refinement, the S-parameters of the ports do not significantly change anymore, meaning change less than Max ΔS , then the iterative process can be considered done. This described iterative process is shown in Figure 4.3.

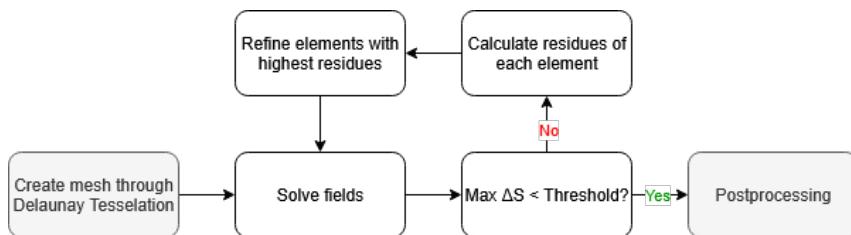


Figure 4.3 Adaptive solution process

4.2 Antennas

In this sections, different antennas are placed in the TEM cell. Their electric and magnetic coupling is investigated through dipole moments. All antennas are fed with a power of 1 MW. Their material are made of a perfect electric conductor. Different positions and offsets are investigated and the results discussed. They are fed through a round wave port with a diameter of 0.4 mm. Its impedance has been normalized to 50Ω .

Describe how the use of normalization of ports influences results.

Short HFSS introduction with boundary conditions, ports and modal and terminal solutions?

4.2.1 Inverted F-antenna

The inverted F-antenna (IFA) is modeled in Ansys HFSS as shown in Figure 4.4. It is positioned at the center of the TEM cell, mounted at the top surface. The 5 mm long wire points towards waveport 2. The excitation is a modal wave port. With a maximum dimension of 5 mm, the antenna is electrically small for a frequency of up to 6 GHz, at which it will be a tenth of the wavelength. In this simulation, the antenna is investigated for the frequency of 100 MHz to 1 GHz. The TEM cell has a width of 40 mm and a height of 24 mm and an impedance of $\sim 50 \Omega$. The goal is to find equivalent dipole moments of the antenna.

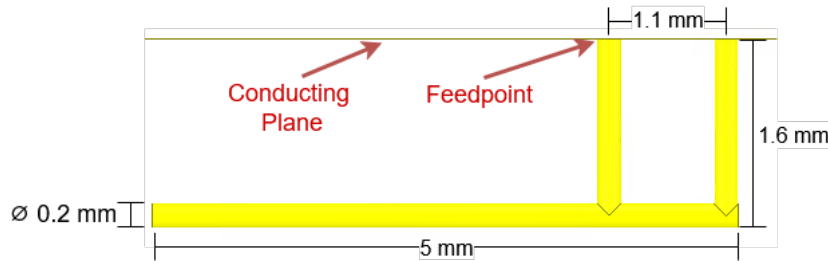


Figure 4.4 Inverted F-antenna used in the simulation

The coupling between the antenna and the two ports of the TEM cell are described by S-parameters, specifically the forward transmission coefficients S_{A1} and S_{A2} . Figure 4.5 shows the magnitude of this coefficient, which is the same for the antenna to both ports ($|S_{A1}| = |S_{A2}|$).

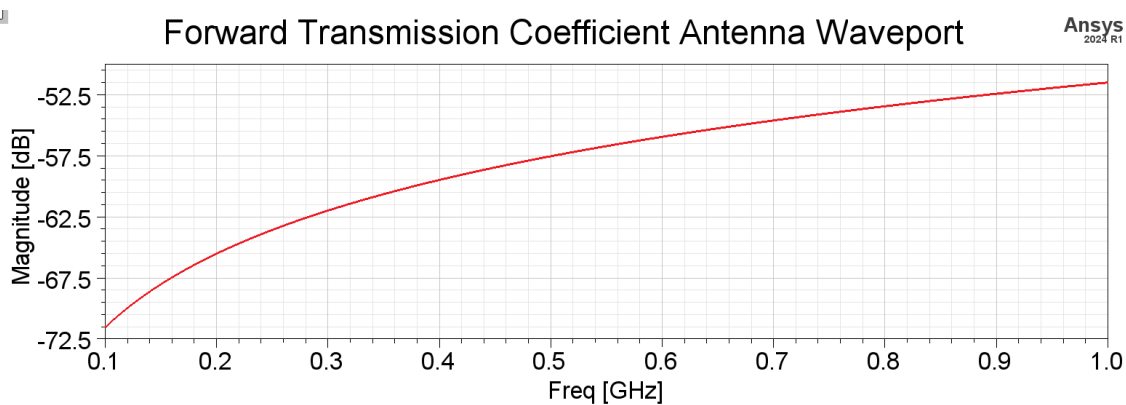


Figure 4.5 S-parameter describing coupling of antenna to waveport 1

$$P_{\text{Antenna}} = \frac{P_{\text{Out1}}}{10^{|S_{A1}|/10}} = \frac{P_{\text{Out2}}}{10^{|S_{A2}|/10}} \quad (81)$$

Equation 81 describes the relation between the input power at the antenna and the measured output power of the TEM cell. It is defined by the magnitude of the forward transmission coefficients.

$$\iint_A \mathbf{e}_0 \times \mathbf{h}_0 \cdot d\mathbf{A} = 1 \quad (82)$$

Equation 82 shows that the electric field \mathbf{e}_0 and magnetic field \mathbf{h}_0 are normalized to $1/\sqrt{W}$. The surface area A , over which the fields are integrated, is that of the output ports of the TEM cell. The field can be linearly scaled by the complex coefficients a and b , which has been described in Equation 39 and Equation 40. Only one pair of such coefficients is needed, since only the TEM mode is considered.

The coefficients a and b have the unit \sqrt{W} . The fields \mathbf{e}_0 and \mathbf{h}_0 are not known over the whole area. However, the electric field \mathbf{e}_0 has only to be known at one specific point in order to determine the equivalent dipole moments, as will be shown here. The normalization condition therefore leads to an output power equal to $|a|^2/2$ or $|b|^2/2$, respectively, which was also found in [32].

$$P_{\text{out1}} = \iint_A \langle \mathbf{S} \rangle \cdot d\mathbf{A} = \iint_A \frac{1}{2} \Re\{(a \cdot \mathbf{e}_0) \times (a \cdot \mathbf{h}_0^*)\} \cdot d\mathbf{A} = \frac{|a|^2}{2} \quad (83a)$$

$$P_{\text{out2}} = \iint_A \langle \mathbf{S} \rangle \cdot d\mathbf{A} = \iint_A \frac{1}{2} \Re\{(b \cdot \mathbf{e}_0) \times (b \cdot \mathbf{h}_0^*)\} \cdot d\mathbf{A} = \frac{|b|^2}{2} \quad (83b)$$

The phase shifts of S_{A1} and S_{A2} differ, which is shown in Figure 4.6. The difference of these phase shifts influences the quantity of magnetic dipole moment and electric dipole moments. A large phase shift indicated a large magnetic dipole moments compared to the electric dipole moment, and vice versa. The large difference in phase shifts in Figure 4.6 lets one expect the first case. However, the phase shift does not influence the overall output power. It is incorporated into the coefficients a and b , by multiplying the term $e^{i\varphi_a}$ or $e^{i\varphi_b}$ to their magnitude. The phase shift of each port is then implemented by φ_a at the port of the coefficient a , and by φ_b at the port of the coefficient b .

The Poynting vector is periodic from $-\pi/2$ to $\pi/2$, hence any phase difference above that value must be corrected by adding π to it.

The output power of each port is then derived through Equation 83a and Equation 83b. So if $|a| = |b| = 1$, then the electric field \mathbf{e}_0 may be measured, when the output power at one port is $\frac{1}{2} W$. Because it is assumed that the TEM cell contains only waves in the TEM mode, the normalization of the electric and magnetic fields can be used to simplify the calculations.

$$\mathbf{e}_0 \times \mathbf{h}_0 = \Re\{\mathbf{e}_0 \times \mathbf{h}_0^*\} \quad \text{for TEM mode} \quad (84)$$

By using Equation 43 and Equation 42, the equivalent dipole moments are derived. Because of Lorentz reciprocity theorem, only fields aligned with the dipole moments get to the output ports. Since only the TEM mode propagates, only the electric dipole moment in z-direction and the magnetic dipole moment in y-direction influence the fields. If higher order modes can propagate, the other dipole moments become relevant, too.

Problem with large TEM cell: Formula does not work for large frequencies. The field distributes around

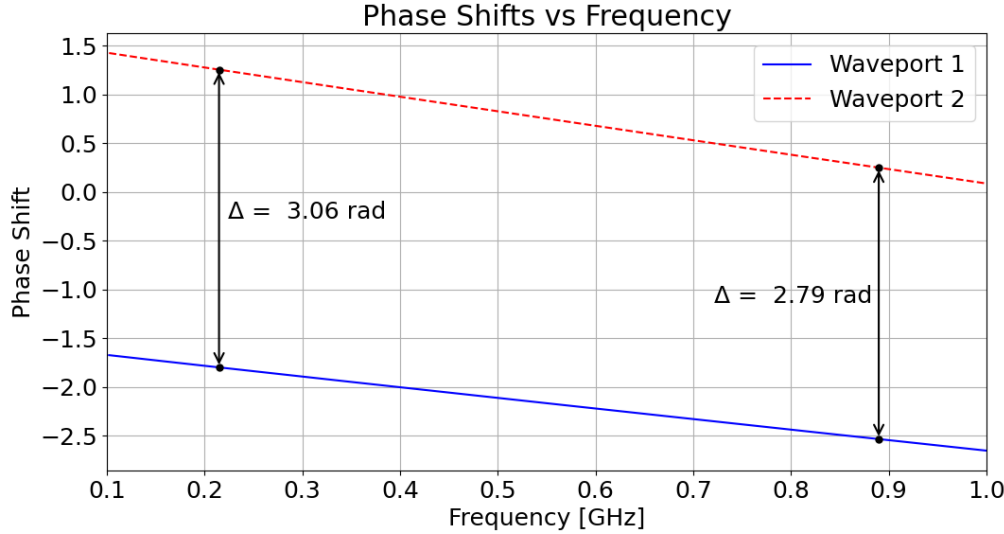


Figure 4.6 Phase of S-parameters from antenna to waveport 1 and 2

$$m_e = \frac{a + b}{e_{0,z}} \quad (85)$$

$$m_m = i \frac{a - b}{k_0 e_{0,z}} \quad (86)$$

By adding or subtracting the coefficients a and b , the dipole moments are expressed into the handy Equation 85 and Equation 86. There, $k_0 = \frac{2\pi}{\lambda}$ is the free space wave number and $e_{0,z}$ is the normed electric field in z-direction at middle height between septum and the upper wall of the TEM cell. However, the height of the measurement point is not important, as the electric field is uniformly distributed along the z-axis. Additionally, the x- and y-components of the electric field \mathbf{e}_0 are zero, which leads to these equations. The dipole moments m_e and m_m are defined to be in the center of the TEM cell, at middle height. If they are shifted in any direction, their approximation would not hold true anymore.

Figure 4.7 shows the measurement point of $e_{0,z}$. This wouldn't work if the magnetic and electric dipole wasn't defined to be exactly at a height of $b/4$, at dead center. The Lorentz Reciprocity theorem used to derive the formulas take the cross product of the electric field traveling to one output port with the magnetic field caused by the dipole, minus the magnetic field traveling to the same output port minus the electric field caused by the dipole. Since the dipoles are in dead center, the electric field caused by the dipole does only have a z-component, and the magnetic field caused by the dipole only a y-component. If this was not the case, the other components would have to be taken into account of the fields at the test point. They would already have disappeared at the output ports due to the long travel, and the Lorentz Reciprocity theorem becomes more cumbersome to use.

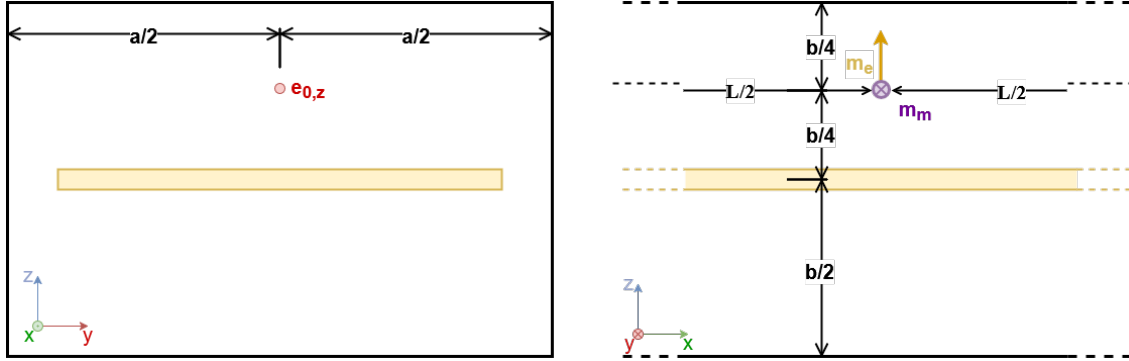


Figure 4.7 Dipole moments and measurement point of $e_{0,z}$ in TEM cell

By placing the dipoles in dead center, it is possible to measure the electric field at the output port and normalize it to $\frac{1}{2} \text{ W}$.

Using Equation 18 the magnetic dipole moment can be expressed as a magnetic current. The resulting $m_{m,\text{mag}}$ is shown in Equation 87. The phase shift between the magnetic and electric dipole moments m_{ez} and $m_{my,\text{mag}}$ is always $\frac{\pi}{2}$, which generates the desired TEM wave pattern.

Write clearer.
And put into theoretical part.

$$m_{m,\text{mag}} = im_m \omega \mu_0 \quad (87)$$

The antenna may then be replaced with those two dipole excitations in the center of the upper half of the TEM cell. The magnitude and phase of the fields, as well as the output powers, should remain the same as in the case with the antenna. The phase shift may be determined by measuring the phase shifts of the electric fields at both output ports. When applying this described method in a measurement with a real TEM cell, the phase shift may be found by adding and subtracting the output powers of both ports, as is shown in [25].

Figure 4.8 shows the dipole moments over frequency. The electric dipole moment m_e has been normalized to the free-space wave impedance of 377Ω to make the dipole moments comparable. This is possible because the dipole moments are interchangeable through the wave impedance [12, p. 414]. The antenna input power has been set to 142588.47 W , because this leads to an output power of 1 W at a frequency of 1 GHz . The magnetic dipole moment is much larger than the electric dipole moment, because the current loop of the antenna is aligned with the TEM cell's magnetic fields, but the line current is not with the TEM electric fields. The magnetic dipole moments rises linearly with the frequency, which is equal to a quadratic increase of power. Only the TEM modes has been considered in the simulation, as other modes disturb the calculations.

Is this
CFM or
IFA simu-
lation?

The electric field \mathbf{e}_0 is approximated with Equation 88 for the purpose of interpolation over frequencies and analytical analysis. The constant u is a scaling factor, which must be adjusted to fit the real electric field values. In this case, this constant equals $u = 820.34$. The left-hand side term $|a| \cdot e_{0,z}$ is the overall electric field at the measurement point according to Equation 39. Figure 4.9 shows the resulting plot.

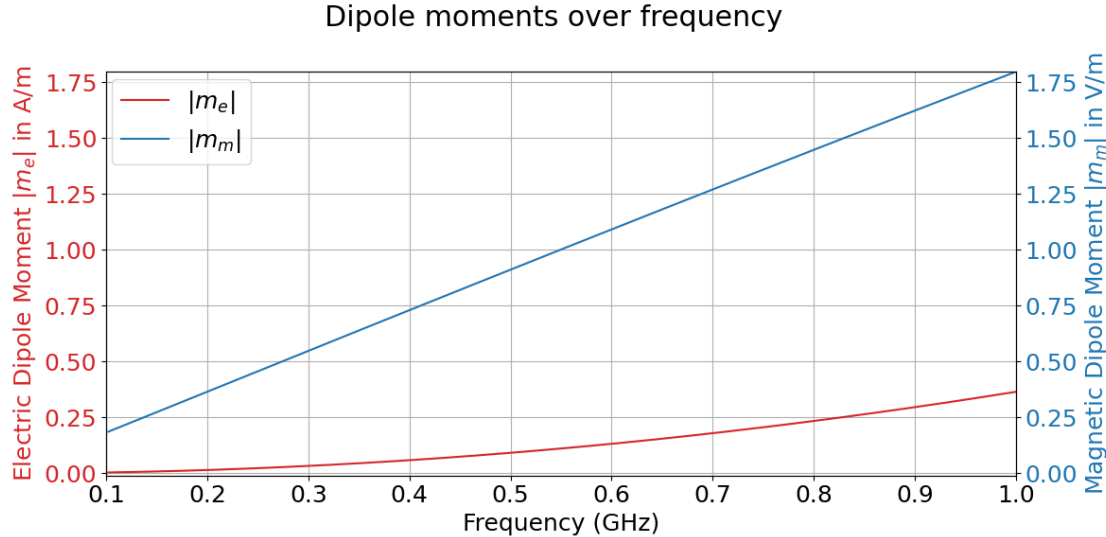


Figure 4.8 Dipole moments over frequency

$$|a| \cdot e_{0,z} = \sqrt{2P_{\text{Out}}} \cdot e_{0,z} = u\sqrt{P_{\text{Out}}} \frac{V}{m \cdot \sqrt{W}} \quad (88)$$

The electric field can also be approximated by Equation 89, where $b/2 = 12$ mm is half the height and $Z_W \approx 50 \Omega$ is the impedance of the TEM cell. This works for TEM cells with thin septum. The constant u can be adjusted to fit this equation. The term $\sqrt{2}$ is needed to convert the effective value of the electric field into its magnitude.

$$|a| \cdot e_{0,z} = \frac{\sqrt{2 \cdot P_{\text{Out}} \cdot Z_W}}{b/2} \quad (89)$$

The magnetic coupling with the septum happens due to the alignment of the current loop with the magnetic field of the dominant TEM mode. The antenna is now rotated by 90° around the z-axis, such that the magnetic current loop stands perpendicular to the magnetic TEM fields. Figure 4.10 demonstrates the phase of the S-parameters, describing the coupling of antenna to waveport 1 and 2. Since the magnetic dipole moment is responsible for a phase between the ports, Figure 4.10 strongly hints to an absence of it.

?? shows that the electric dipole moment m_e has stayed the same, while the magnetic dipole moment became zero. Consequently, the overall power transfer between the antenna and the waveports is also much lower.

Repeat for different orientations?
Change variable name:
TEM cell height.

The same procedure was repeated with different dipole moments positions, for which Equation 59b

Electric field approximation and Output Power over frequency

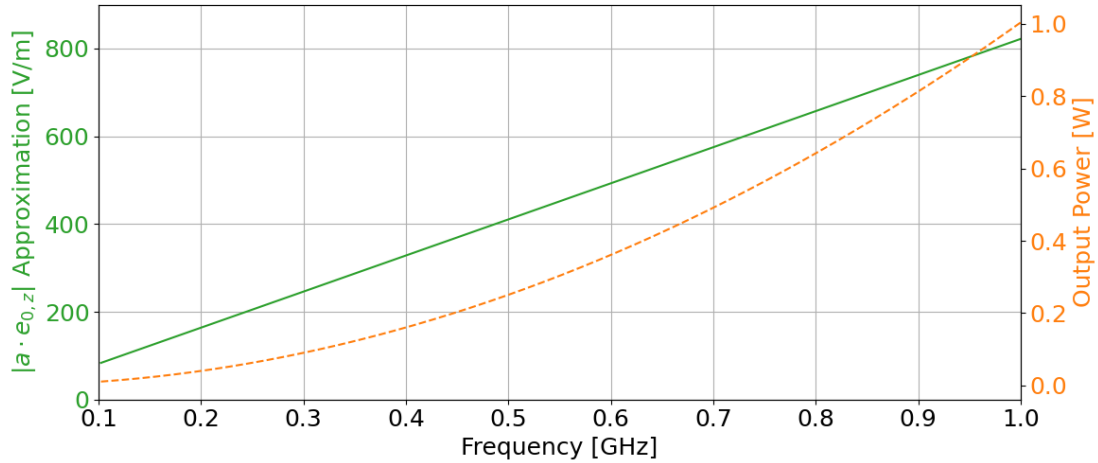


Figure 4.9 Output power and electric field over frequency

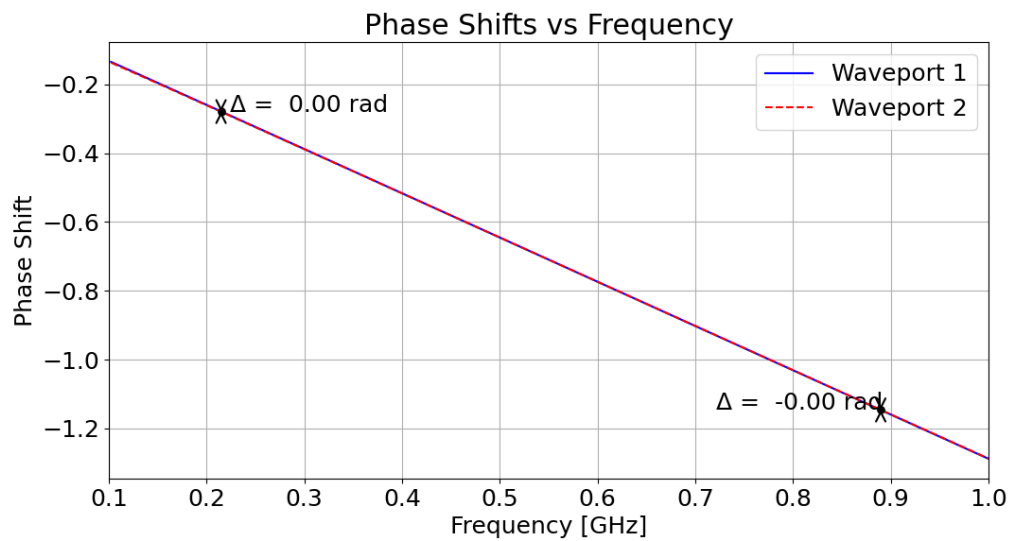


Figure 4.10 Phase of S-parameters from rotated antenna to waveport 1 and 2

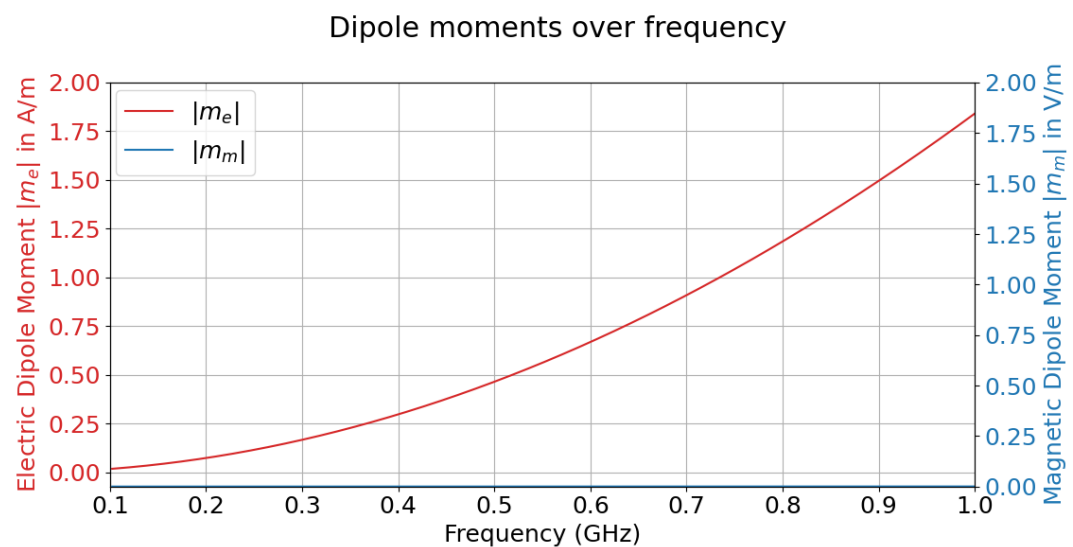


Figure 4.11 Dipole moments of rotated antenna

4.2.2 Center Fed Monopole Antenna

The center fed monopole antenna is shown in Figure 4.12. The conducting plane in Figure 4.12 is on the top side of the TEM cell, thus the image is rotated counter-clockwise by 90 degrees. The electric wire with the length of 5 mm points towards the septum. The 1.1×1.6 mm loop is again aligned with the magnetic field lines of the TEM mode. The antenna is fed with a power of $P_{\text{Antenna}} = 127770.39$ W, which once more leads to an output power of $P_{\text{Out}} = 1$ W at 1 GHz at both output ports.

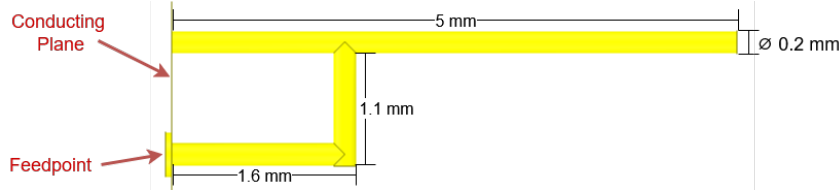


Figure 4.12 Center fed monopole antenna used in simulation

The magnitude of $|S_{A1}| = |S_{A2}|$ in Figure 4.13 shows stronger coupling. As will be seen below, this is because of an increased electric dipole moment, while the magnetic dipole moment remained the same. Therefore, the center fed monopole antenna couples well electrically with the TEM cell.

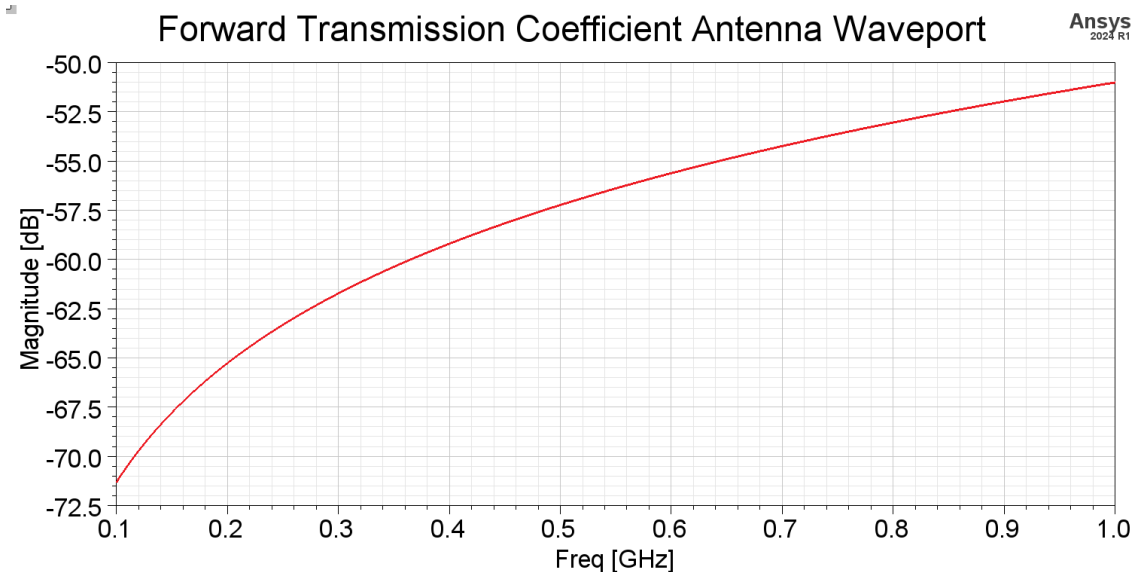
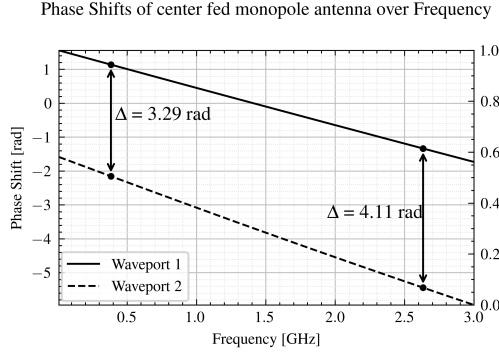
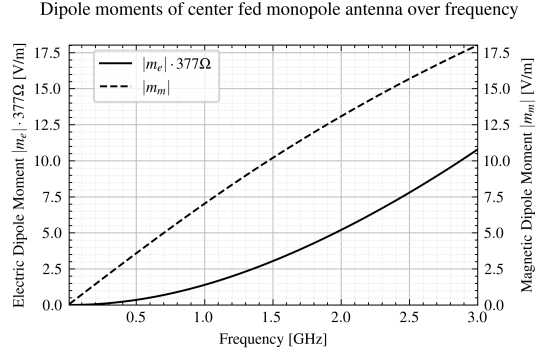


Figure 4.13 S-parameter describing coupling of antenna to waveport 1

Figure 4.15 shows that the magnetic dipole moments of the inverted F and center fed monopole antennas are equal. This is due to the same size of the current loops. However, the electric dipole moments increased for the center fed monopole antenna. The alignment of the line current with the TEM cell's electric field causes this. (antenna power = 126549.7191667088 W)

The output power has been scaled as in the simulation before. This leads to the same

**Figure 4.14** Phase shift**Figure 4.15** Dipole moments

electric field magnitude. Therefore, the electric field and output power over frequency plot are the same as in the case for the inverted F antenna, visible in Figure 4.9.

When rotating this antenna by 79° , the electric and magnetic dipole moment influence the output power by roughly the same amount, as visible in ???. This makes itself manifest by a phase shift of around 45° between the output powers of the waveports. Interestingly, both the electric and the magnetic dipole moment demonstrate a non-linear behavior.

4.2.3 Monopole Antenna

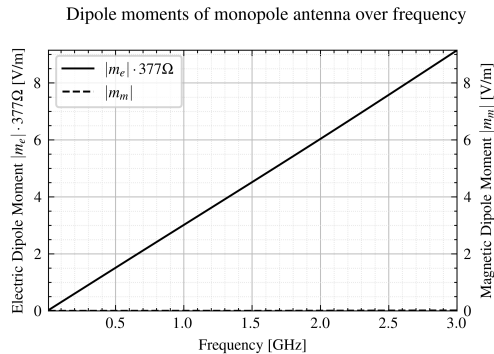
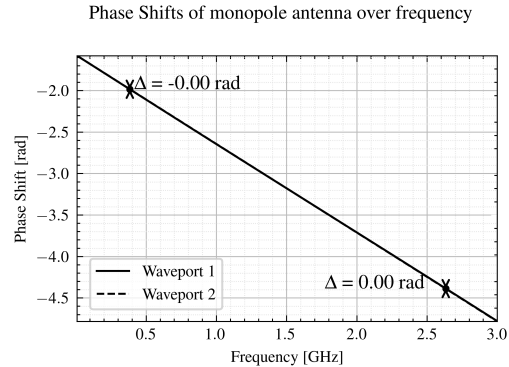
**Figure 4.16** Dipole moments**Figure 4.17** Phase shift

Figure 4.16 shows the dipole moments of the monopole antenna. Note the linear relation of the electric dipole moment m_e to the frequency, which is not given in the center fed monopole and inverted-F antenna. The magnetic dipole moment equals zero, which is explainable by the very weak coupling of the magnetic fields. The length of the monopole antenna is 5 mm.

The wave impedance in the near field region is very high in the low frequencies, but sharply drops off with frequency. The relation is approximately given by Equation 90, where r describes the distance to the antenna. Generally, the near-field is electric, which is explaining by the capacitive behavior of the monopole antenna. The decrease of the

Why does the magnetic moment sink?

CFM at 90° rotation still demonstrates magnetic dipole moment, opposed to current loop. Does this scale with antenna height, i.e. electric dipole moment?

the length goes to 2mm

insert plot

Source: Wikipedia. Date: 16.01.2024

wave impedance over the frequency also leads to better impedance matching, as the source impedance is set to 50Ω . This leads to better power transfer, and more efficient radiation.

$$|Z_w| \approx 60\Omega \frac{c}{r \cdot f} \quad (90)$$

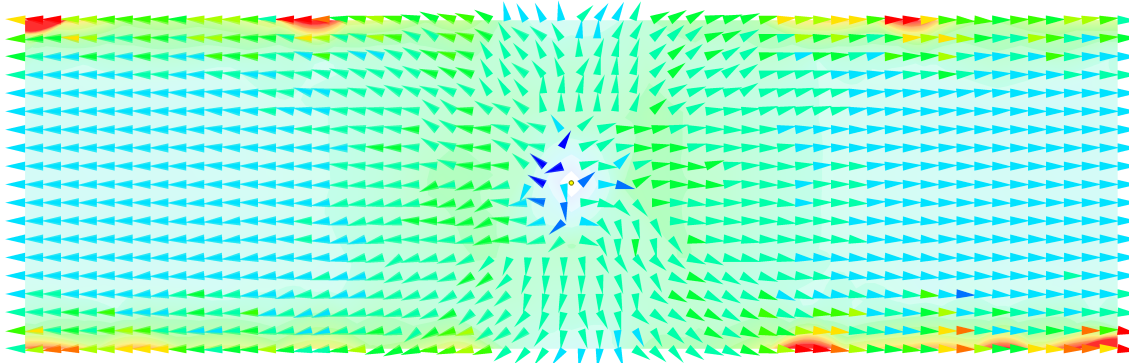


Figure 4.18 Current surface density at 550 MHz

?? shows the induced surface currents on the septum, when giving the monopole antenna an offset of 7.5 mm. The energy transfer decreases by 1 dB.

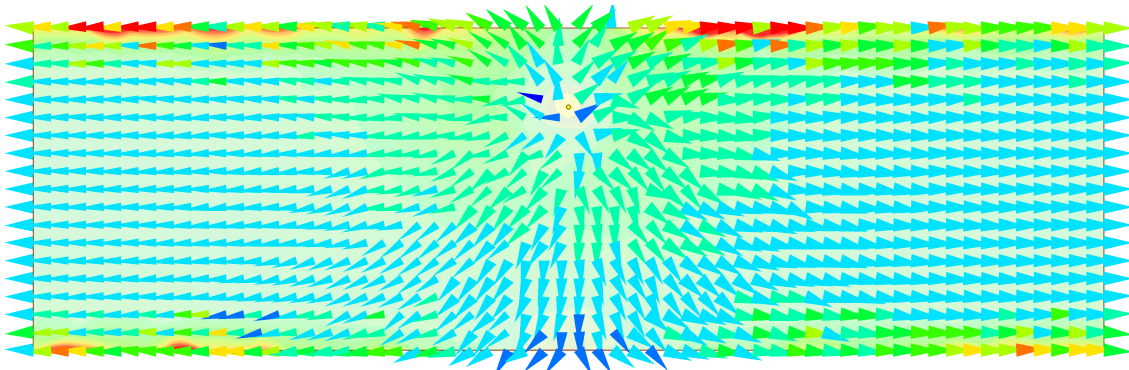


Figure 4.19 Current surface density at 550 MHz with offset

Figure 4.22 demonstrates the feed current over the frequency. Because the monopole antenna has a high impedance, the it rises linearly with the frequency. Meanwhile, the voltage falls quadratically with the frequency . This all fits together with the quadratic rise of the radiation resistance . This evaluation has been done automatically through a script, integrating the magnetic field around the wire .

An equivalent circuit is derived in Figure 4.20, which is known as Chu equivalent circuit for a short dipole [10].

The distribution of the current along the monopole antenna is numerically derived by integrating the magnetic field strength in a closed loop around the antenna. Figure 4.21

Explain how much of the power transfer is due to the quadratic rise of the radiation resistance, and how much of it is due to better matching. As visible, in the current / voltage plots, the quadratic rise of the resistance influences the power transfer much more than the increased matching.

show plot and show mathematically

show mathematically?

How big is the radius of the closed

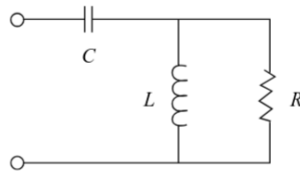


Figure 4.20 Chu equivalent circuit of short dipole

shows approximately a linear decrease of the current along the antenna, as assumed in [??](#). A stronger decrease is visible near the feedpoint, which might occur due to the large displacement current density. An option to improve upon this simulation is increasing the feedpoint size, such that it has 50Ω impedance without needing port normalization.

Maybe increase resolution by adding more steps

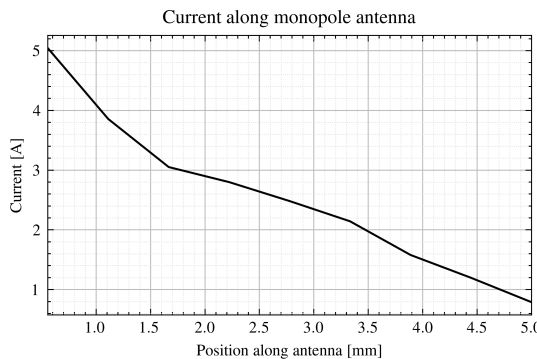


Figure 4.21 Current distribution

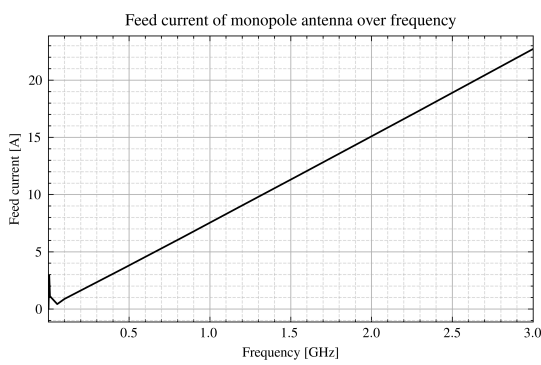


Figure 4.22 Feed current

4.2.4 Loop antenna

equivalent circuit in Balanis page 244

inductance of square loop given in Balanis page 245

A loop antenna of dimensions in form of a square is constructed, with each side having a length of 1.6 mm. This is preferable to a really round antenna, because the adaptive meshing models it much more accurate. The antenna is oriented such that the highest amount of magnetic fields enters it.

Maybe describe this in the HFSS theory part?
Modeling of round surfaces.

Figure 4.23 shows the dipole moments of the loop antenna over frequency. As expected, the magnetic dipole moment m_m contributed the largest amount to the antenna coupling. A small amount of electric dipole moment is also present, which naturally occurs due to the current wire aligned with the TEM electric fields. The electric dipole moment m_e increases non-linearly with frequency.

why?

Note that the surface current density in Figure 4.24 is much more concentrated in the center. In the case of the monopole antenna, the current density distributed almost equally around the septum. In the case of the loop antenna, the current below the antenna seems to be cut off by the rotational eddy currents next to them. Furthermore, the phase shift

Find reasons for the eddy current to exist.
Maybe

Dipole moments of loop antenna over frequency

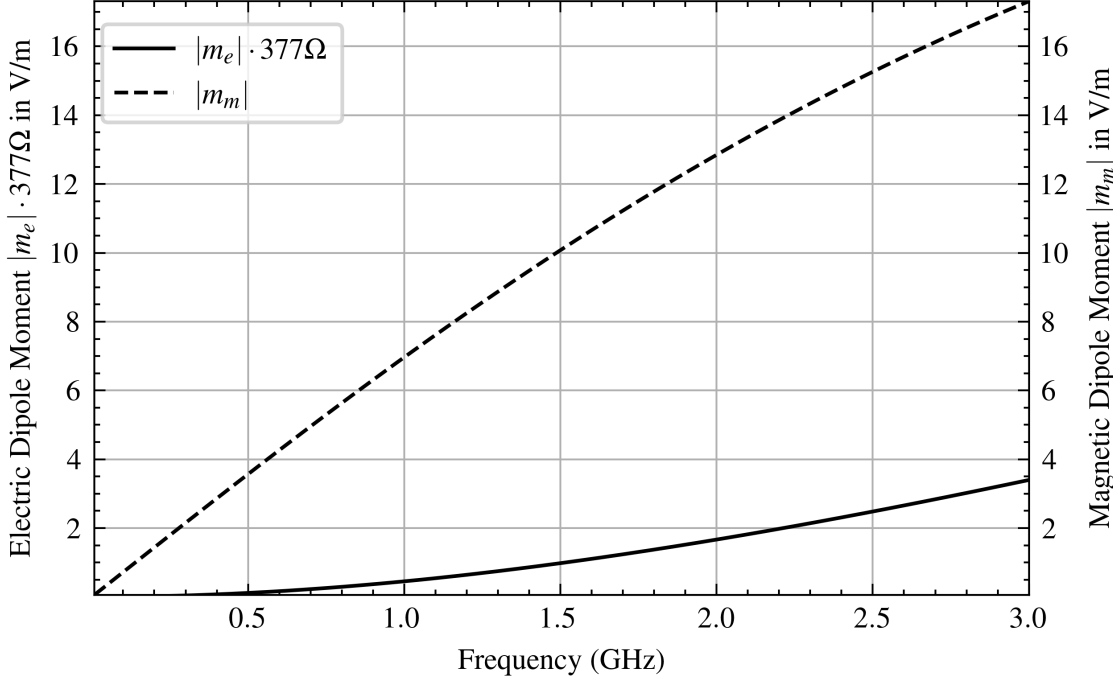


Figure 4.23 Dipole moments of loop antenna

between the currents at the output ports is 180° , leading to the perceived phase shift of magnetic dipole moments.

Figure 4.25 demonstrates the surface current density when shifting the loop antenna 7.5 cm (quarter of the septum width) in y-direction. The coupling and transferred energy remains roughly the same.

Figure 4.26 shows the surface current density when rotating the antenna by 90° . Only a negligible amount reaches the output ports, leading to no coupling.

Figure 4.27 shows the current distribution of the current loop antenna, when it is rotated and contains an offset. Again, the eddy currents dominate. However, some of those currents propagate towards the output ports, increasing the energy transfer minimally (0.5 dB). Additionally, the energy transferred is in phase, which makes it indistinguishable from an electric dipole.

Figure 4.28 shows the charge density distribution in the current loop antenna. Charges collect, among other locations, at the bottom wire. This leads to electric coupling with the septum.

The current and voltage drops along the wire are not constant. From the feedpoint to the first corner, there is a much larger voltage drop and current, than from the second corner to the ground plane. Consequently, the power consumed by the first part is much higher

 annotate
maximum
and minimum
current densities

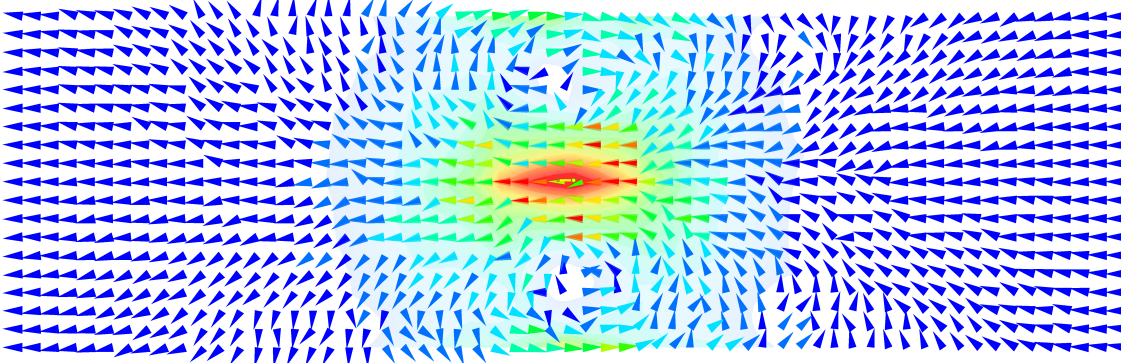


Figure 4.24 Surface current density at 550 MHz

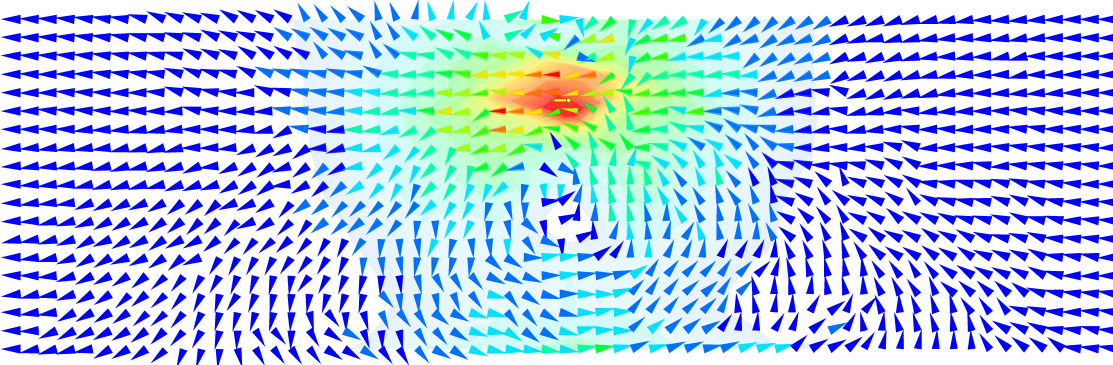


Figure 4.25 Surface current density at 550 MHz with offset

than by the latter. Additionally, this difference in power consumption increases slightly over frequency.

The electric current reduces over the wire because of the displacement current to the septum and the ground plane. As visible in the charge density plot in Figure 4.29 and the electric field plot in Figure 4.30, much of the displacement current occurs near the feedpoint and at the wire parallel to the septum. Consequently, this is where the current drops by the most amount.

Figure 4.33 and Figure 4.32 show the current and voltage consumption of the antenna. The phase shift equals $\phi \approx 89.80^\circ$, which hints to a strong inductive behavior. The inductance is determined to be $L \approx 2.15 \text{ nH}$. The capacitance is very low, but does lead so some displacement current. The frequency behavior of the voltage and current interchange if the antenna is strongly capacitive, as it the case in a monopole antenna.

Next, the electric and magnetic near field is investigated. The wave impedance $Z = E/H$ shown in Figure 4.34 in the center of the loop rises linearly over frequency. At low frequencies, the wave impedance is very low, which confirms the inductive behavior of the antenna. However, as the frequency increases, so does the voltage drop. This may be analogous to a inductor in an electrical circuit, across which the voltage drop also increases with frequency $U = iL\omega I$.

Insert power consumption plots of each antenna section

Insert current distribution plots

H-field from other perspective?

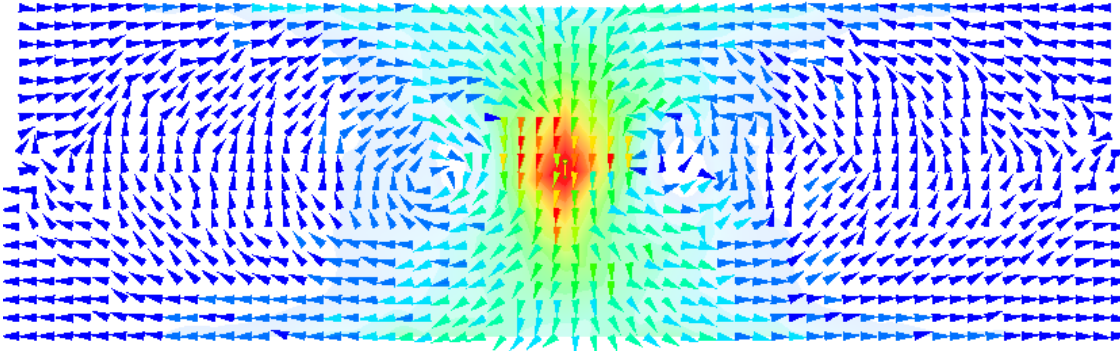


Figure 4.26 Surface current density at 550 MHz with rotated antenna

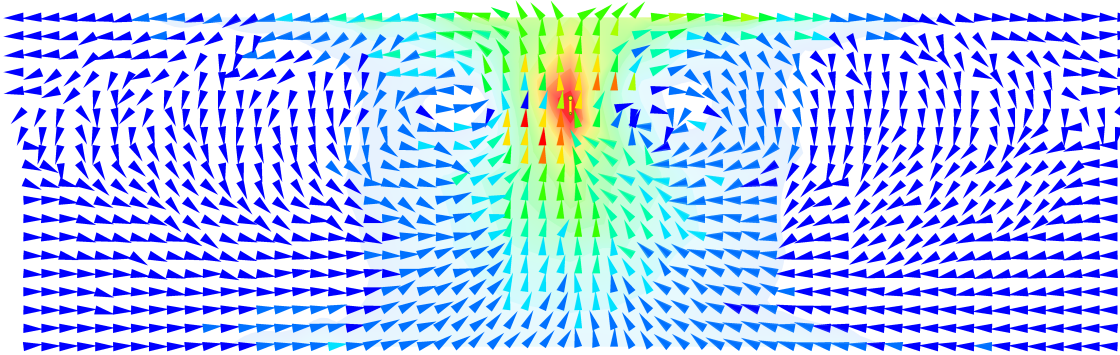


Figure 4.27 Surface current density at 550 MHz with offset and rotated antenna

Equation 58 relates the dipole moments to the output power. The influence of the dipole moments is determined by the electric field at the electric dipole moment and the magnetic field at the magnetic dipole moment. In this formula, the electric and magnetic field are simply related through the free-space wave impedance. However, as visible in Figure 4.34, the wave impedance at the location of the dipole moments (i.e. at the antenna) is much lower. Additionally, it rises linearly with the frequency. This influence of the antenna itself on the fields around the dipoles could explain the non-linear relation of the dipole moments to the frequency.

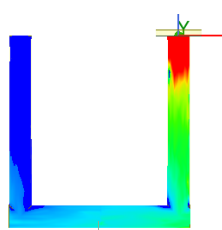


Figure 4.28 Charge density distribution in current loop antenna

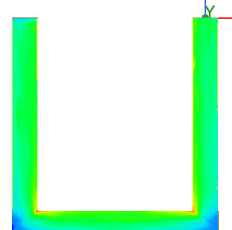


Figure 4.29 Current density distribution in current loop antenna

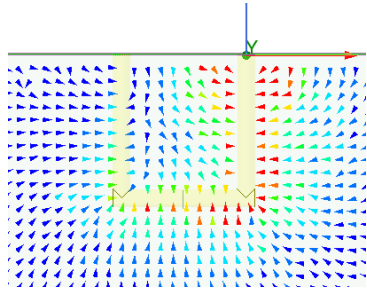


Figure 4.30 Electric near field in current loop antenna

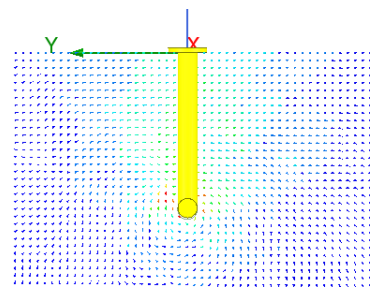


Figure 4.31 Magnetic near field in current loop antenna

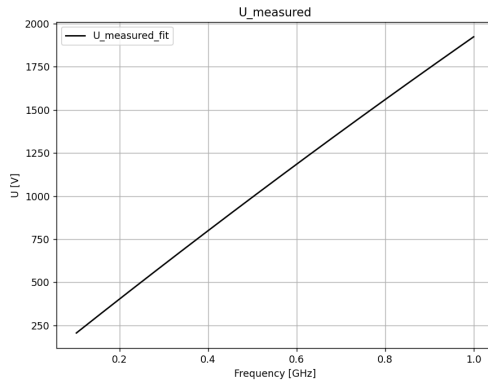


Figure 4.32 Voltage drop at feed point of current loop antenna

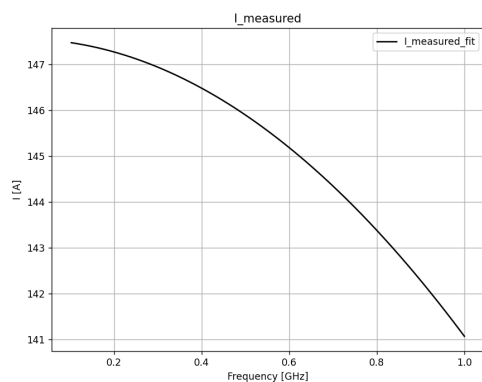


Figure 4.33 Current consumption at feed point of current loop antenna

Figure 4.35 shows the power consumption of the antenna, which is influenced by two factors. The radiation resistance rises quadratically with the frequency. At the same time, the impedance increases, leading to higher matching and therefore to a higher power transfer. This is contrary to the monopole antenna, where the impedance decreases over the frequency, again leading to better impedance matching, because the impedance was high to begin with. The source impedance is 50Ω .

Figure 4.36 shows the total power maintained in the system, meaning $S_{11}^2 + S_{12}^2 + S_{13}^2$. It does not add up to one, meaning that some energy is lost due to finite conductivity of the septum and antenna. This energy dispersion increases with frequency, most likely due to a decrease of the conductivity due to high-frequency effects like the Skin-effect. Consequently, the power consumption in Figure 4.35 shows a square root relation to the frequency, because the power dispersion is so high. When changing the material of the antenna and septum to a perfect electric conductor, the total power in a system remains one (no power is dispersed) and the power consumption over frequency of the antenna shows a quadratic relation to the frequency, due to the quadratic increase of the radiation resistance.

The Skin-effect reduces the area in which the current flows, therefore increasing resistance. This appears due to the reduction of the depth, in which the electromagnetic waves enter.

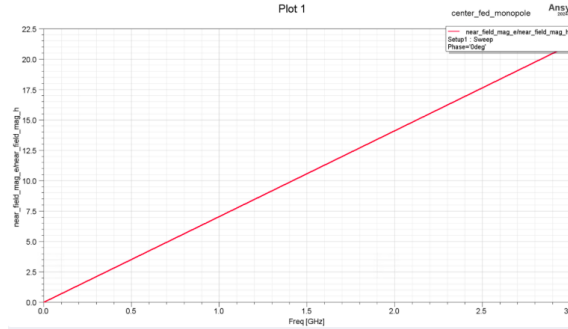


Figure 4.34 Wave impedance in the center of the loop

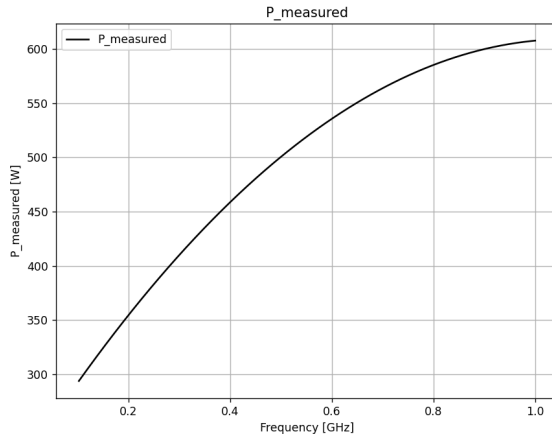


Figure 4.35 Power consumption of the current loop antenna

It is also called Skin depth and mathematically described by Equation 91b. It depends on the imaginary part of the wave number κ , which is described in Equation 91a. For high conducting materials ($\sigma \gg \epsilon\omega$), the dependency of the skin depth d on the frequency can be described therefore as $d \propto 1/\sqrt{\omega}$. Since the power dispersion is linearly proportional to the area of the conductor and therefore Skin-depth, it shows the same dependency on the frequency $P_{\text{disp}} \propto 1/\sqrt{\omega}$ [8].

$$\kappa = \omega \sqrt{\frac{\epsilon\mu}{2}} \left[\sqrt{1 + \left(\frac{\sigma}{\epsilon\omega} \right)^2} - 1 \right]^{1/2} \quad (91a)$$

$$d = 1/\kappa \quad (91b)$$

At 1 GHz, the dispersed power already equals to 0.46 %, which is much higher than the power transfer of the antenna to one waveport of 1.26e-5 at that frequency. Because this dispersed power is proportional to the square-root of the frequency $P_{\text{disp}} \propto 1/\sqrt{\omega}$, the overall transferred power to the antenna shows the same characteristic. However, the power transfer to the waveports has a quadratic dependency on the frequency.

This dispersed power may be ignored in the simulations by changing the antenna's mate-

Own little chapter for skin effect?
Loop antennas are known for higher conductor losses than radiation
Balanis page 231

explain better.

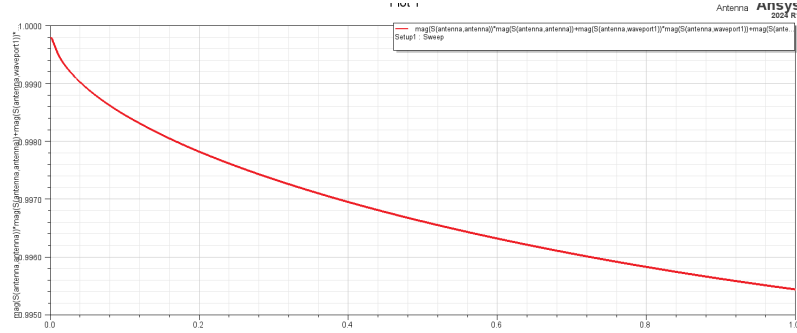


Figure 4.36 Total power distribution in the system

rial (main source of power dissipation) and the septum from copper to a perfect electric conductor. The overall power in the system then remains at a constant one over the whole frequency range. Additionally, the transferred power to the antenna now has a quadratic relationship with the frequency, indicating increased radiation efficiency, previously described by Equation 10.

The current-loop antenna contains two electric dipoles, shifted in phase by 180° . They therefore oppose each other in the power transfer to the waveports. However, as visible in the electric near field plot in Figure 4.32, the electric dipole moment from node A to the feedpoint is much larger than the one from node B to ground. The reason can be demonstrated by representing the antenna with its nodes in ???. The partial inductances in this schematic are much larger than the capacitances. This leads to a large voltage drop between node A and B, and therefore a weaker electric dipole moment at node B.

Additionally, this voltage difference $V_A - V_B$ rises linearly over the frequency, due to the linearly increasing impedance of the inductance $i\omega L$. This means, that the over electric dipole moment a quadratic relationship to the frequency has.

Further, Figure 4.37 shows the wave impedance of the near-fields at the loop antenna. The Equation 58 shows, that the influence of the dipoles depends on the electric and magnetic fields at the dipoles position. The electric and magnetic fields are related through the wave impedance $Z = E/H$. If the wave impedance rises linearly over frequency, the electric field increases over the magnetic fields, giving more influence to the electric dipole moments. As previously discussed, there are two electric dipole moments in this antenna, benefiting from that.

The wave impedance Z_w in the near field of the electrically small loop antenna is approximated by Equation 92. It confirms the linear relationship of the near-field wave impedance to the frequency.

$$|Z_w| \approx 2\pi^2 \cdot 240 \Omega \cdot \frac{r \cdot f}{c} \quad (92)$$

Show plots?

Magnetic moment equivalent antenna. Explain with current and H-field, too

Prove square frequency dependency

Monopole antenna: Also change in wave impedance, but there is not

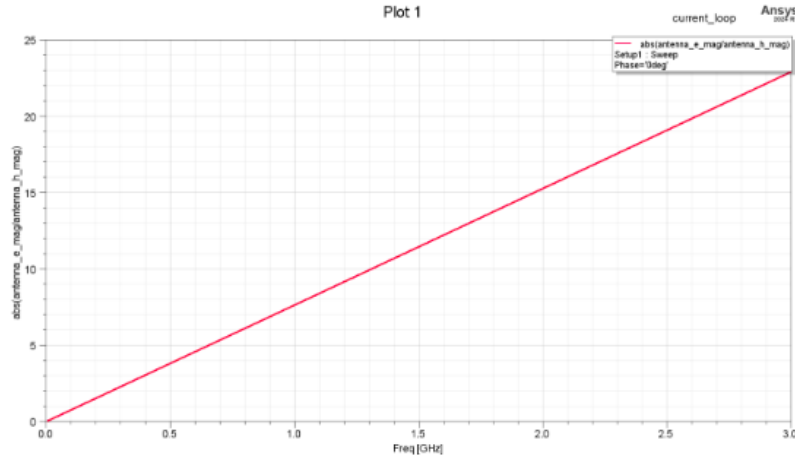


Figure 4.37 Wave impedance in near field of loop antenna over frequency

4.2.5 Serial Loop Antenna

This section will discuss the antenna displayed in Figure 4.38. The idea of that antenna is to create two magnetic dipole moments, which are in phase. As the frequency increases, the displacement current between the loops becomes larger, thus reducing the current through and weakening the second loop. The dipole moments in Figure 4.39 demonstrate a non-linear behavior of the magnetic dipole moment (only very weakly recognizable, but with a geometry sweep this becomes clearer). Also, it would be interesting to measure the wave impedances in both loops over the frequency. Also, find the current distributions, add current plots and electric fields, charge distributions.

Find a geometry where this effect is much stronger

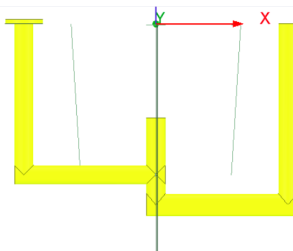


Figure 4.38 Serial loop antenna

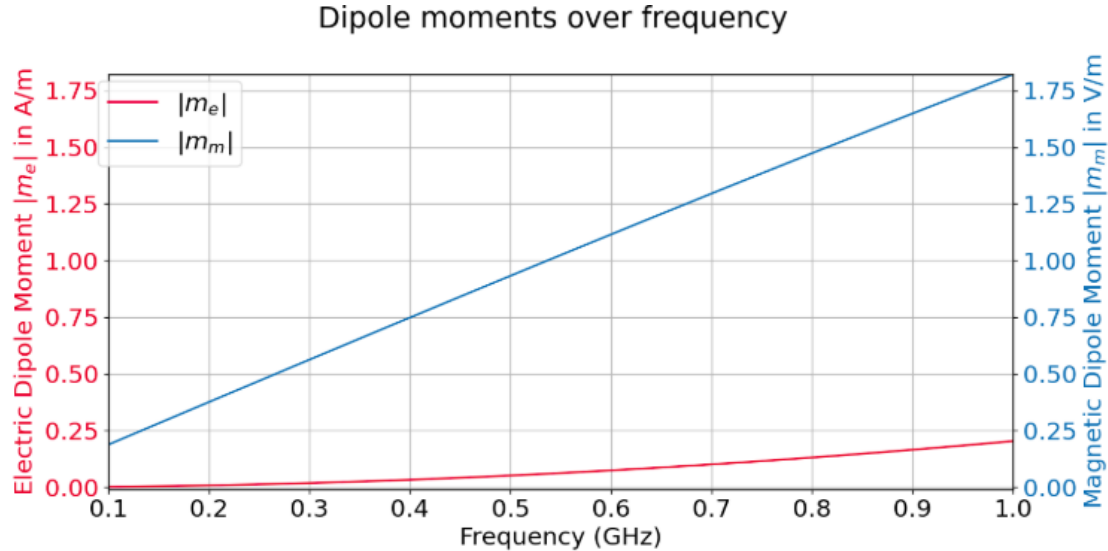


Figure 4.39 Dipole moments

4.2.6 Offset of source antennas and eddy currents

This section is probably wrong.

Next, the CFM is rotated by an angle. This angle is swept from 0° to 90° , iteratively increased by 1° [deg]. At 90° the magnetic dipole moment is at a minimum, while it is the largest at 0° . The idea is now to find a balance between the electric and magnetic dipole moment, such that the antenna operates in a way of resonance. In this operation, the S11 parameter shall be the lowest, even though the coupling of the magnetic field only becomes weaker with increasing angle. The reason for this approach by increasing angle is that it is otherwise very hard to achieve such a balance between the dipole moments by purely scaling the antenna. The electric dipole moment is very weak, and when increasing the antenna height (thus only the electric dipole moment), it soon becomes very large and even touches the septum. Rotating the angle instead becomes a very efficient alternative. This has been determined just by looking at the phase shifts from the antenna to the waveports: If electric and magnetic dipole moments are roughly equally influential, then the phase shift between the ports shall be 90° . Very important for these simulation is the renormalization of the waveports. This enables the port exciting the antenna to have an impedance of 50 Ohm, independent of size. This will make a geometry sweep of the antenna able, without influencing the impedance of the port exciting the antenna (Imagine a coax cable attached to the antenna. It is hinted by the round waveport in the model. When it gets shifted around, its wave impedance changes, and so does the reflection, and the results are distorted)

Figure 4.40 it is visible, that the lowest S11 (least reflections) is achieved at a rotation angle of 72° .

Eddy currents occur on the septum. They increase with frequency. When they get too large, the next-order mode starts propagating. Offsetting the antenna / dipole moment

Relate the offset to the normalized E field distribution. For Example, the vertical part of the current loop antenna does not influence the TEM cell coupling without offset, which can be shown with the normalized E field distribution.

Can the normalized h-field be used?

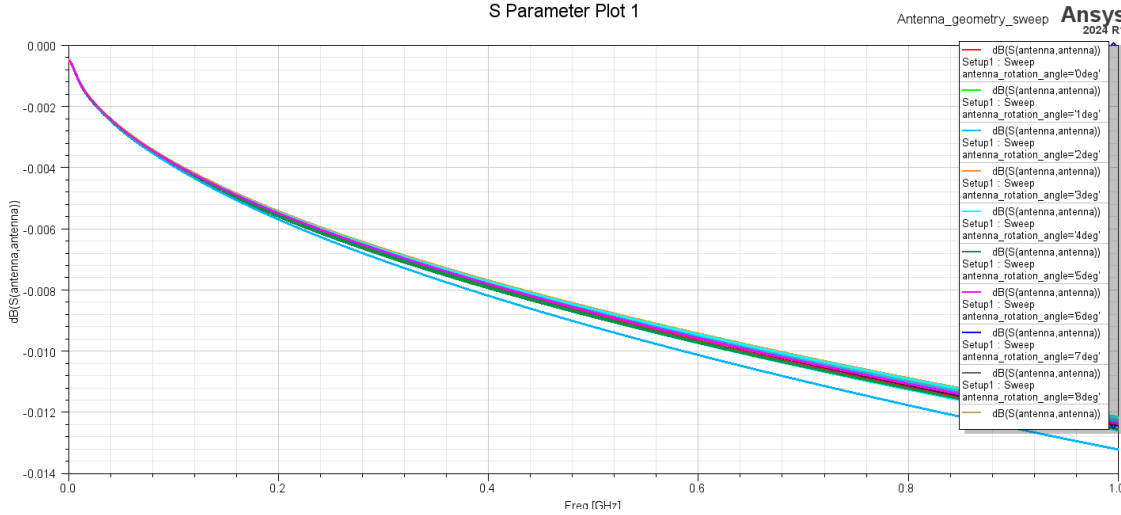


Figure 4.40 CFM S11 sweep with rotation angle stepping

in y-direction reduces the amount of influence of the eddy current on the power carrying current in the septum.

When implementing an offset in the center fed monopole antenna, the coupling between the waveports and the antenna changes. The change is visible in Figure 4.41, although the magnitude of the coupling to both ports is the same.

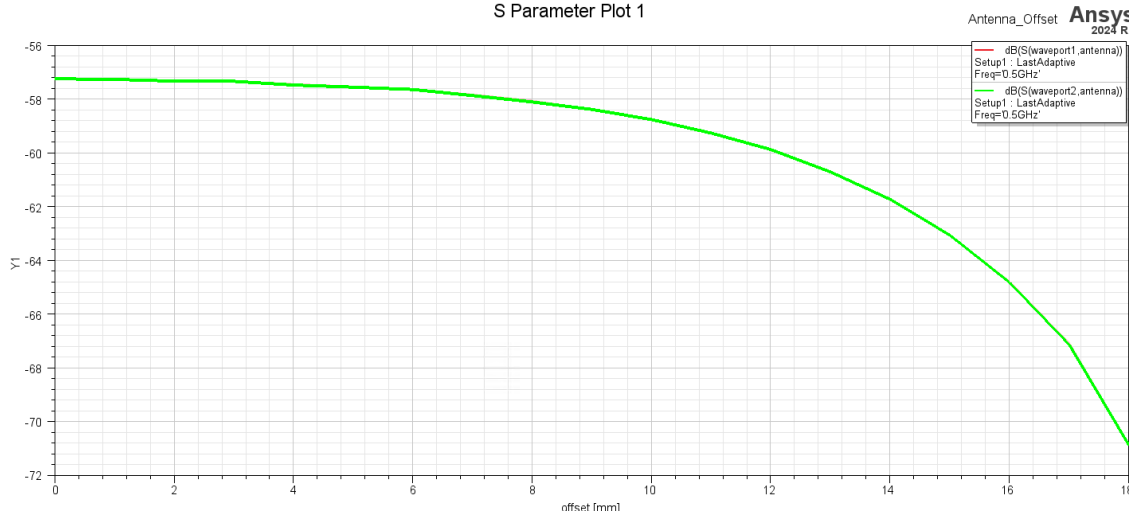


Figure 4.41 Center fed monopole antenna coupling dependence on offset (Delete after)

How does offset influence the eddy currents and the result?

Better investigation of offset: Show coupling and eddy currents

4.3 Dipole Moments

4.3.1 Orientation and position in TEM Cell

Figure 4.42 demonstrates the normalized output power of an electric dipole moment pointing in y-direction, and one in z-direction. This simulation only demonstrates the coupling

behavior of the dipole moments over frequency, to explain the non-linear coupling of certain antennas. If dipole moments in certain positions and orientations couple with a different proportionality than the standard two dipole moments (e_z and m_y), then the non-linear coupling may be explained that way.

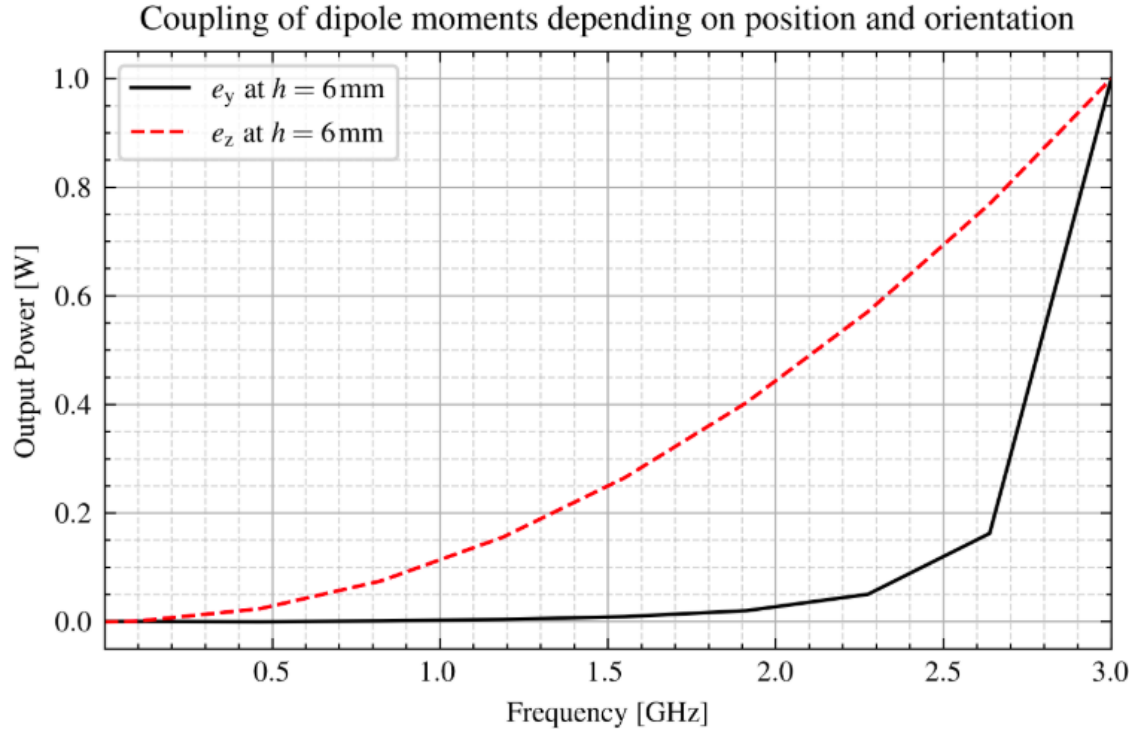


Figure 4.42 Comparison of normalized output power of electric dipole moments

The electric dipole moment in z-direction e_z demonstrates the expected behavior: As the frequency rises, this dipole moment rises linearly and thus increases the output power quadratically. The electric dipole moment in y-direction e_y also increases linearly with frequency, but does not significantly change the output power for the low frequencies. However, as the frequency approaches the cut-off frequency of the next-higher order mode, the coupling rises significantly.

This simulation is repeated where the dipole moments are located at a height of $h = 6\text{ mm}$, which is the dead center of the TEM cell, and $h = 9\text{ mm}$, which is near the top wall of the TEM cell. The simulation results are similar for both cases.

Most importantly, this simulation shows that the dipole moments have a relation to the frequency independent on their position. While their magnitude themselves do depend on the position, the relation to the frequency does not.

Repeat
Simula-
tion
for sev-
eral other
dipole
moment
positions
and ori-
entations?

4.3.2 Combining dipole moments with antennas

4.3.3 Application of dipole moments

As shown in the previous simulations, antennas may be represented by dipole moments. This can be done in simulation models, which would otherwise be computationally too effortful. The dipole moments may be put into a shielded enclosure around a larger electronic system, as has been done in [18].

4.4 Investigation of field regions

In this section, the influence of the field region described in subsection 2.5 on the dipole moments are investigated. Making the TEM cell larger, such that $k \cdot r > 1$, is hardly possible without enabling higher-order modes to propagate. On the other hand, making the TEM cell smaller such that $k \cdot r \ll 1$, proves to be feasible. The following simulations are conducted with a TEM cell of dimensions $a = 10\text{ mm}$ and $b = 6\text{ mm}$, visible in Figure 4.43.

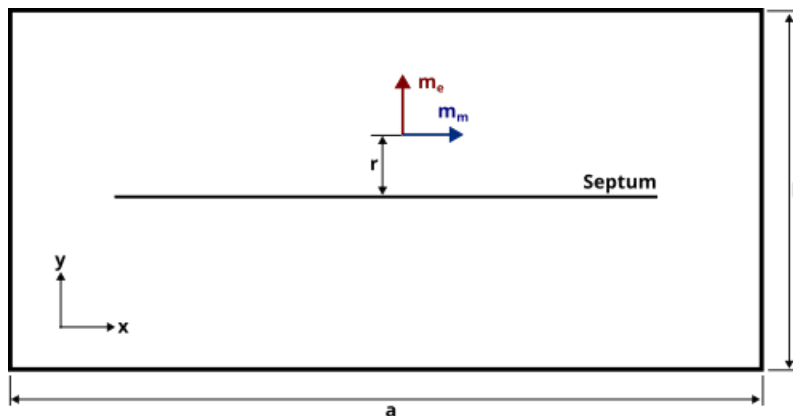


Figure 4.43 TEM cell containing dipole moments

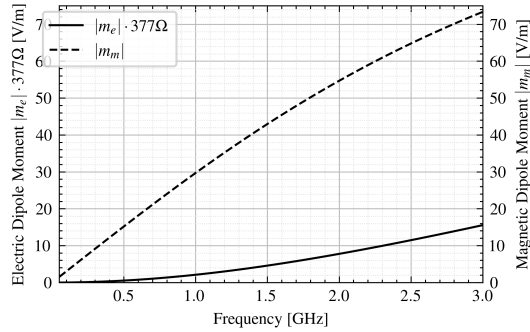
First, the current loop antenna used in subsubsection 4.2.4 is placed in the dead center of the TEM cell. The equivalent dipole moments are shown in Figure 4.44. In the Figure 4.45 next to it, the dipole moments of the same antenna in the larger TEM cell used before ($a = 40\text{ mm}$ and $b = 24\text{ mm}$) are presented.

This is done to compare the dipole moments in both cases. While they clearly increased by magnitude in case of the small TEM cell due to better coupling, their non-linear frequency relation still remains. This means that the change of field regions is not the reason for this behavior.

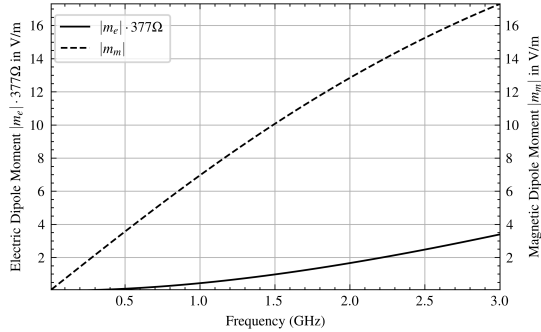
The $k \cdot r$ factor is determined in Figure 4.46 in the frequency range from 1 MHz to 3 GHz for the small TEM cell. This factor does not surpass 0.1, thus fulfilling the requirement $k \cdot r \ll 1$ for this investigation. For comparison, the $k \cdot r$ factor over a wider frequency range are shown in Figure 4.46 for the normal sized TEM cell ($a = 40\text{ mm}$ and $b = 24\text{ mm}$) and a degenerately high TEM cell ($a = 10\text{ mm}$ and $b = 44\text{ mm}$). The high TEM does not have a port impedance of 50Ω , and is an attempt to achieve a large $k \cdot r$ factor without higher-order modes propagating. The markers in Figure 4.47 indicate the cut-off frequency, in

The electric field approximation in the python code is based on the large TEM cell. Therefore, the magnitude of the dipole moments of the small TEM cell

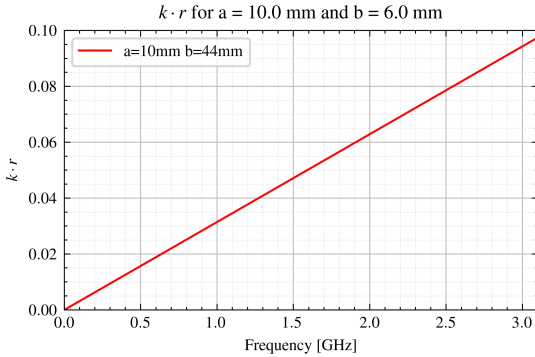
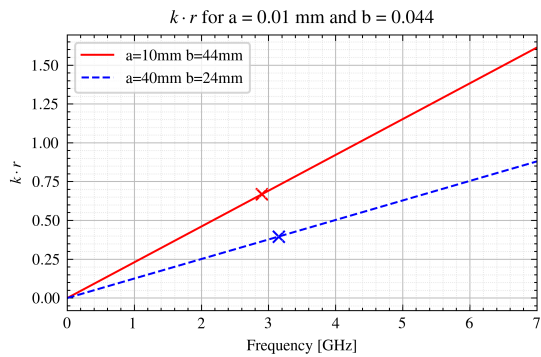
Dipole moments of loop antenna in small TEM cell over frequency

**Figure 4.44** Moments in small TEM cell

Dipole moments of loop antenna over frequency

**Figure 4.45** Moments in normal TEM cell

which the next higher-order mode propagates. They demonstrate, that even in the high TEM cell a $k \cdot r = 1$ is not achieved.

**Figure 4.46** $k \cdot r$ in small TEM cell**Figure 4.47** $k \cdot r$ for other TEM cells

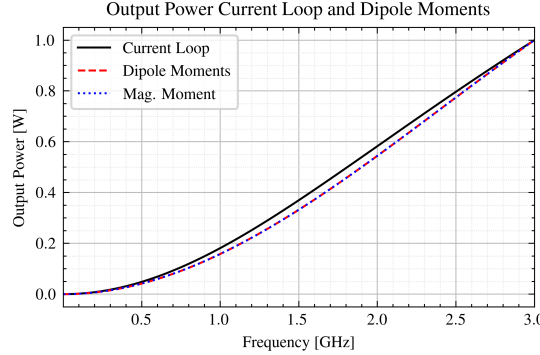
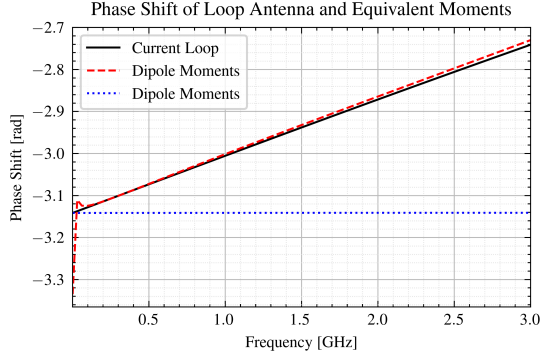
Now, three simulations are conducted with different excitation sources in the small TEM cell:

Fix figures: Titles and Legends

- The current loop
- The equivalent dipole sources e_z and m_m of the current loop
- The equivalent magnetic dipole source m_m , neglecting e_z

Figure 4.48 shows the output power over frequency normalized to 1 W for all three constellations. The normalization is done to qualitatively discuss the frequency-dependent coupling behavior. Figure 4.49 demonstrates the phase shift between the powers at the two waveports over frequency.

The frequency dependent behavior of the output power does not change depending on the type of dipole moment used. This is significant, because this shows that the dipole moments do not exhibit different coupling behaviors in the TEM cells. This is further proven in the phase shift plots. The magnetic dipole moment causes a constant phase

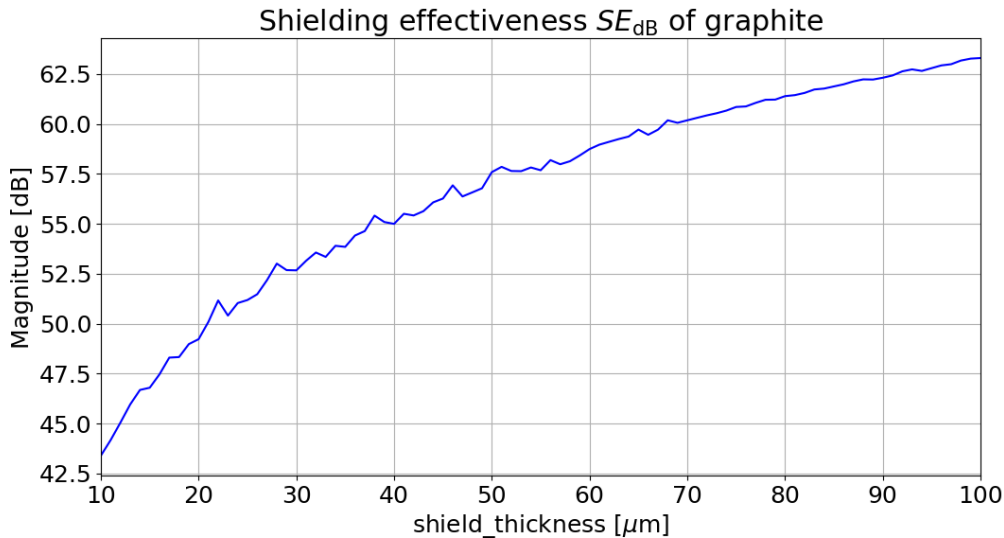
**Figure 4.48** Output powers**Figure 4.49** Phase shifts

shift of $-\pi$. If this was not the case, this would mean that the coupling behavior of the magnetic dipole moment in the TEM cell would change. Since the opposite is the case, this poses as good evidence against arguments of change in field regions causing the non-linear dipole moment behavior. Instead, it is very likely to be caused by the geometry of the antenna.

4.5 Shielding Simulations

4.5.1 Shielding effectiveness of graphite

The reference power P_{ref} has been set to 1 W. Using Equation 71 and the S-parameters from the simulation results, P_{load} may be determined. Figure 4.50 demonstrates the shielding effectiveness of graphite in dB SE_{dB} over the shielding material thickness. The solution frequency is 500 MHz. A frequency sweep shows that the reflection coefficient S_{11} does not depend much on the frequency.

**Figure 4.50** Shielding effectiveness of graphite

I think
the low
SE in the
low shield
thick-

Forward transmission coefficient	Empty aperture	aperture filled with FR408
Waveport 1 to 3 S_{13}	-83.80 dB, -144.96°	-85.27 dB, -155.79°
Waveport 1 to 4 S_{14}	-90.31 dB, -144.96°	-87.14 dB, 25.00°

Table 2 Forward transmission coefficients

The components of SE_{dB} are determined according to Equation 62.

4.5.2 Shield effectiveness of FR4

The FR4 has a relative permittivity of $\epsilon_r = 4.4$. According to Equation 64, the relative wave impedance is $Z = 0.476$. This leads to a reflection coefficient of $R = -0.355$ by Equation 63.

The reflection coefficient $|S_{11}| = 0.045$.

4.5.3 Dual TEM Cell

A simulation setup of a dual TEM cell is created. A rectangular aperture with a side length of $l = 5\text{ cm}$, inspired by [30], connects both TEM cells. One waveport 1, as in Figure 3.11, is excited with a power of $P = 1\text{ W}$. The simulation is conducted, leaving the aperture open. A second one determines the coupling of the waveports, when the aperture is filled with a graphite sheet with a thickness of $t = 50\text{ }\mu\text{m}$.

At a frequency of $f = 500\text{ MHz}$, the coupling between waveport 1 to the waveports 3 and 4 of the receiving TEM cell is shown in Table 2. Only one frequency point is investigated, as the results stay roughly constant over the inspected frequency range from 100 MHz to 1 GHz.

Using Equation 72a and Equation 72b leads to the shielding effectiveness for electric coupling $SE_{dB}^e = 19.07\text{ dB}$ and magnetic coupling $SE_{dB}^m = -9.22\text{ dB}$. To get the sum P_{sum} and difference P_{diff} of powers, the phase of the signals have to be considered. With unit input power at the transmitting TEM cell, Equation 93a and Equation 93b are used for this purpose [25].

$$P_{sum} = (S_{13} + S_{14})(S_{13} + S_{14})^* \quad (93a)$$

$$P_{diff} = (S_{13} - S_{14})(S_{13} - S_{14})^* \quad (93b)$$

Indicated by the phase shift of roughly 180° , the coupling between the TEM cells occur mainly due to magnetic dipoles. Due to the relative permittivity of $\epsilon_r = 3.66$ and the relative permeability of $\mu_r \approx 1$ of the shielding material, the magnetic fields dominate. This leads to a energy transfer mainly due to magnetic dipole moments. The overall shielding effectiveness SE_{dB} = Equation 94.

$$P_{total} = |S_{13}|^2 + |S_{14}|^2 \quad (94)$$

Why -8dB difference in empty aperture?
Explained in [30]

negative SE possi-ble? Redo Simula-tions with finer Mesh around aperture

One port receives overall more power due to the material. Is it because of

References

- [1] Constantine A. Balanis. *Advanced Engineering Electromagnetics*. John Wiley Sons, 2012.
- [2] Constantine A. Balanis. *Antenna theory: Analysis and design. Buch Constantine A. Balanis*. 3rd. Wiley, 1997.
- [3] Z. Cendes and D. Shenton. “Adaptive mesh refinement in the finite element computation of magnetic fields”. In: *IEEE Transactions on Magnetics* 21.5 (1985), pp. 1811–1816. DOI: 10.1109/TMAG.1985.1063929.
- [4] Z.J. Cendes. “Vector finite elements for electromagnetic field computation”. In: *IEEE Transactions on Magnetics* 27.5 (1991), 3958–3966. DOI: 10.1109/20.104970.
- [5] Z.J. Cendes and J.-F. Lee. “The transfinite element method for modeling MMIC devices”. In: *1988., IEEE MTT-S International Microwave Symposium Digest* (1988), 623–626. DOI: 10.1109/mwsym.1988.22111.
- [6] Robert E. Collin. *Field theory of guided waves*. IEEE Press, 2015.
- [7] Saju Daniel and Sabu Thomas. “Shielding Efficiency Measuring Methods and Systems”. In: *Advanced Materials for Electromagnetic Shielding: Fundamentals, Properties, and Applications*. 2019, pp. 61–87. DOI: 10.1002/9781119128625.ch4.
- [8] David J. Griffiths. *Introduction to electrodynamics*. Cambridge University Press, 2024.
- [9] C. Groh et al. “TEM waveguides for EMC measurements”. In: *IEEE Transactions on Electromagnetic Compatibility* 41.4 (1999), pp. 440–445. DOI: 10.1109/15.809846.
- [10] Robert C. Hansen and Robert E. Collin. *Small antenna handbook*. Wiley, 2013.
- [11] K.H. Huebner et al. *The Finite Element Method for Engineers*. A Wiley-Interscience publication. Wiley, 2001. ISBN: 9780471370789. URL: <https://books.google.at/books?id=f3MZE1BYq3AC>.
- [12] John David Jackson. *Classical Electromagnetics*. 2nd ed. Wiley.
- [13] J.P. Karst, C. Groh, and H. Garbe. “Calculable field generation using TEM cells applied to the calibration of a novel E-field probe”. In: *IEEE Transactions on Electromagnetic Compatibility* 44.1 (2002), pp. 59–71. DOI: 10.1109/15.990711.
- [14] M. Koch, C. Groh, and H. Garbe. “Exact Determination of Resonant Frequencies in TEM Cells”. In: *13th International Zurich Symposium and Technical Exhibition on Electromagnetic Compatibility*. 1999, pp. 653–658. DOI: 10.23919/EMC.1999.10791592.
- [15] Galen H Koepke. In: *Theory and measurements of radiated emissions using a TEM cell* (1989). DOI: 10.6028/nist.tn.1326.
- [16] Dominik Kreindl et al. “Evaluation of an analytical equivalent Hertzian dipole representation in tem cells applying the finite element method”. In: *IEEE Transactions on Magnetics* 60.3 (2024), 1–4. DOI: 10.1109/tmag.2023.3324698.
- [17] Dominik Kreindl et al. “Fundamental investigation of wave propagation inside IC-striplines upon excitation with Hertzian dipole moments”. In: *Electronics* 11.16 (2022), p. 2488. DOI: 10.3390/electronics11162488.
- [18] Dominik Kreindl et al. “Measurement and Simulation Methodology for Characterizing the Shielding Effectiveness of Coating Materials for Optical Sensors”. In: *2023 International Symposium on Electromagnetic Compatibility – EMC Europe*. 2023, pp. 1–6. DOI: 10.1109/EMCEurope57790.2023.10274360.

- [19] J.-F. Lee, D.-K. Sun, and Z.J. Cendes. “Full-wave analysis of dielectric waveguides using tangential vector finite elements”. In: *IEEE Transactions on Microwave Theory and Techniques* 39.8 (1991), pp. 1262–1271. DOI: [10.1109/22.85399](https://doi.org/10.1109/22.85399).
- [20] J.F. Lee, D.K. Sun, and Z.J. Cendes. “Tangential vector finite elements for electromagnetic field computation”. In: *IEEE Transactions on Magnetics* 27.5 (1991), pp. 4032–4035. DOI: [10.1109/20.104986](https://doi.org/10.1109/20.104986).
- [21] Paul Lorrain and Dale R. Corson. *Electromagnetic fields and waves*. W.H. Freeman, 1970.
- [22] M.F.N. Mohsen. “Some details of the Galerkin Finite Element Method”. In: *Applied Mathematical Modelling* 6.3 (1982), 165–170. DOI: [10.1016/0307-904x\(82\)90005-1](https://doi.org/10.1016/0307-904x(82)90005-1).
- [23] Cristian MORARI and Cristian BĂLAN. In: *Methods for determining shielding effectiveness of materials* (2015).
- [24] D. Shenton and Z. Cendes. “Three-dimensional finite element mesh generation using Delaunay tessellation”. In: *IEEE Transactions on Magnetics* 21.6 (1985), 2535–2538. DOI: [10.1109/tmag.1985.1064165](https://doi.org/10.1109/tmag.1985.1064165).
- [25] Ippalapalli Sreenivasiah, David Chang, and Mark Ma. “Emission characteristics of electrically small radiating sources from tests inside a tem cell”. In: *IEEE Transactions on Electromagnetic Compatibility* EMC-23.3 (1981), 113–121. DOI: [10.1109/temc.1981.303930](https://doi.org/10.1109/temc.1981.303930).
- [26] GILBERT STRANG. *Analysis of the finite element method*. WELLESLEY-CAMBRIDGE Press, 2018.
- [27] Son Xuat Ta, Ikmo Park, and Richard W. Ziolkowski. “Crossed Dipole Antennas: A review”. In: *IEEE Antennas and Propagation Magazine* 57.5 (2015), pp. 107–122. DOI: [10.1109/MAP.2015.2470680](https://doi.org/10.1109/MAP.2015.2470680).
- [28] John C Tippet, David C Chang, and Myron L Crawford. In: *An analytical and experimental determination of the cutoff frequencies of higher-order te modes in a Tem cell* (1976). DOI: [10.6028/nbs.ir.76-841](https://doi.org/10.6028/nbs.ir.76-841).
- [29] C.M. Weil and L. Gruner. “High-order mode cutoff in rectangular striplines (short papers)”. In: *IEEE Transactions on Microwave Theory and Techniques* 32.6 (1984), 638–641. DOI: [10.1109/tmtt.1984.1132745](https://doi.org/10.1109/tmtt.1984.1132745).
- [30] Perry F Wilson. In: *Excitation of a tem cell by a vertical electric Hertzian dipole* (1981). DOI: [10.6028/nbs.tn.1037](https://doi.org/10.6028/nbs.tn.1037).
- [31] Perry F. Wilson, David C. Chang, and Mark T. Ma. “Input Impedance of a Probe Antenna in a TEM Cell”. In: *IEEE Transactions on Electromagnetic Compatibility* EMC-26.4 (1984), pp. 154–161. DOI: [10.1109/TEMC.1984.304216](https://doi.org/10.1109/TEMC.1984.304216).
- [32] Perry F. Wilson and Mark T. Ma. “Shielding-Effectiveness Measurements with a Dual TEM Cell”. In: *IEEE Transactions on Electromagnetic Compatibility* EMC-27.3 (1985), pp. 137–142. DOI: [10.1109/TEMC.1985.304277](https://doi.org/10.1109/TEMC.1985.304277).
- [33] Perry F. Wilson and Mark T. Ma. “Simple approximate expressions for higher order mode cutoff and resonant frequencies in TEM cells”. In: *IEEE Transactions on Electromagnetic Compatibility* 28.3 (1986), 125–130. DOI: [10.1109/temc.1986.4307269](https://doi.org/10.1109/temc.1986.4307269).